Icarus 211 (2011) 472–497

Contents lists available at ScienceDirect

Icarus

journal homepage: www.elsevier.com/locate/icarus

Origin of the structure and planform of small impact craters in fractured targets: Endurance Crater at Meridiani Planum, Mars

Wesley A. Watters [a,*], John P. Grotzinger [b], James Bell III [a], John Grant [c], Alex G. Hayes [b], Rongxing Li [d], Steven W. Squyres [a], Maria T. Zuber [e]

[a] Department of Astronomy, Cornell University, Ithaca, NY 14853, USA
[b] Division of Geological and Planetary Sciences, California Institute of Technology, Pasadena, CA 21125, USA
[c] National Air and Space Museum, Smithsonian Institution, Washington, DC 20013, USA
[d] Department of Civil and Environmental Engineering and Geodetic Science, Ohio State University, Columbus, OH 43210, USA
[e] Department of Earth, Atmospheric and Planetary Sciences, Massachusetts Institute of Technology, Cambridge, MA 02139, USA

ARTICLE INFO

Article history:
Received 29 March 2010
Revised 12 August 2010
Accepted 18 August 2010
Available online 19 September 2010

Keywords:
Impact processes
Mars, Surface
Geological processes

ABSTRACT

We present observations and models that together explain many hallmarks of the structure and growth of small impact craters forming in targets with aligned fractures. Endurance Crater at Meridiani Planum on Mars (diameter ≈ 150 m) formed in horizontally-layered aeolian sandstones with a prominent set of wide, orthogonal joints. A structural model of Endurance Crater is assembled and used to estimate the transient crater planform. The model is based on observations from the Mars Exploration Rover Opportunity: (a) bedding plane orientations and layer thicknesses measured from stereo image pairs; (b) a digital elevation model of the whole crater at 0.3 m resolution; and (c) color image panoramas of the upper crater walls. This model implies that the crater's current shape was mostly determined by highly asymmetric excavation rather than long-term wind-mediated erosion. We show that modal azimuths of conjugate fractures in the surrounding rocks are aligned with the square component of the present-day crater planform, suggesting excavation was carried farther in the direction of fracture alignments. This was previously observed at Barringer Crater in Arizona and we show the same relationship also holds for Tswaing Crater in South Africa. We present models of crater growth in which excavation creates a "stellate" transient cavity that is concave–cuspate in planform. These models reproduce the "lenticular-crescentic" layering pattern in the walls of some polygonal impact craters such as Endurance and Barringer Craters, and suggest a common origin for tear faults and some crater rays. We also demonstrate a method for detailed error analysis of stereogrammetric measurements of bedding plane orientations.

1. Introduction

The field of impact crater geology began with the investigations of D.M. Barringer in the first decade of the 20th century, when he identified several hallmarks of impact processes at the crater that now bears his name (Barringer, 1905): (a) an inverted stratigraphy in the upper rim walls above the pre-impact horizon (the "overturned flap"); (b) the uplift of strata that are flat-lying in the far-field; and (c) meteoritic material distributed over the surrounding area. This study began a decades-long debate about the origins of Barringer Crater (also known as "Meteor Crater"), resolved in favor of an impact origin by Gene Shoemaker's detailed geological analysis. Shoemaker (1960) compared nuclear explosion craters and Barringer Crater, noting several features in common: (a) a circumferential overturned synclinal fold; (b) debris that preserves an inverted stratigraphic sequence in the upper fold limb (the overturned flap); and (c) crater floors covered with allochthonous debris (a "breccia lens"). Subsequent investigations identified similar features at the Odessa Crater in west Texas (Shoemaker and Eggleton, 1961; Evans, 1961; Evans and Mear, 2000), Lonar Crater in India (Lafond and Dietz, 1964; Maloof et al., 2009), and small craters in northern and western Australia (Milton and Michel, 1965; Milton, 1968; Guppy et al., 1971; Shoemaker et al., 2005). Additional structures were described at Barringer and other craters such as inter-thrust wedges, distinctive patterns of thrust-faulting and tear faults (Shoemaker, 1960; Roddy, 1978; Poelchau et al., 2009), as well as asymmetries in rim uplift, extent of overturning, and bedding strike, which may indicate the impact azimuth (Shoemaker et al., 2005; Poelchau et al., 2009). Signs of shock metamorphism were noticed by Barringer (1905) but were not understood until the 1960s, when these became widely regarded as the most diagnostic signature of an impact origin (Chao et al., 1960; Hörz, 1968; Carter, 1968).

* Corresponding author.
E-mail address: wesley.andres.watters@gmail.com (W.A. Watters).

0019-1035/$ - see front matter © 2010 Elsevier Inc. All rights reserved.
doi:10.1016/j.icarus.2010.08.030

A core drilling study at the Brent crater in Ontario, Canada (Dence, 1968) was used to resolve an outstanding paradox: small-scale laboratory experiments in sand and low-strength targets (e.g., Gault et al., 1968; Stoeffler et al., 1975; Piekutowski, 1977) reveal the overturned synclinal fold and inverted stratigraphy on crater flanks, but not the breccia lens on the crater floor, which in large craters significantly lowers the ratio of depth to diameter. Dence (1968) found that allochthonous debris in the breccia lens did not exhibit the high degree of shock metamorphism found in ejected materials, and therefore was not derived from fallout. The authors proposed the idea of a "transient crater" opened by the excavation flow and preserved in small-scale experiments, but which in larger craters is modified as the unstable upper walls slump into the crater floor, forming a breccia lens. For the present study, the notion of a transient crater is very important because the hinge of the overturned flap is formed before the earliest stage of modification and slumping (Melosh, 1989). The flap hinge is therefore a relict structure whose planform imitates the transient crater shape.

Some of the subsequent geological analysis of simple craters has focused on the description of faulting and fracturing caused by the cratering flow and subsequent, early-stage modification. Faults occur in four main types: (a) shallow-to-steeply dipping over-thrusts, dipping craterward, in which the upper block moves away from the crater: e.g., at Barringer Crater (Kring, 2007), Odessa Crater (Shoemaker and Eggleton, 1961; Evans, 1961), and observed in laboratory experiments (Gault et al., 1968); (b) rotated thrust, normal, and reverse faults associated with crater wall uplift, dipping $\leqslant 45^\circ$ away from the crater, in which the upper block is displaced craterward with respect to the lower block: e.g., at Barringer Crater (Shoemaker and Eggleton, 1961) and Lonar Crater (Maloof et al., 2009); (c) steeply-dipping or listric normal faults in which the upper block moves craterward, caused by slumping of the transient crater walls: e.g., at Lonar Crater (Maloof et al., 2009); and (d) tear faults formed when adjacent blocks are uplifted by different amounts: e.g., at Barringer Crater (Shoemaker, 1960; Roddy, 1978).

Shoemaker (1960) suggested that crater excavation is more efficient along pre-existing planes of weakness to account for the roughly square shape of Barringer Crater, which formed in sedimentary rocks with a regionally-extensive conjugate set of orthogonal joints that bisect the crater corners. This was supposedly confirmed by a small number of laboratory experiments (mentioned but not shown in Gault et al. (1968)), although these results were never followed up. The conclusions of Shoemaker (1960) were later supported by the detailed measurements of Roddy (1978). The observations of Fulmer and Roberts (1963) based on a large number of explosion crater experiments confirmed that small craters forming in comparatively indurated targets with well-developed fracture systems have highly polygonal shapes, while craters forming in unconsolidated sediments or weakly-indurated rocks are highly circular. Recent work has shown that the observed distribution of crater planforms is reproduced by a model of crater growth in which the growth radius is a simple function of the influence of discrete strength heterogeneities in a given direction (Watters, 2009). Poelchau et al. (2009) proposed that fracture-bounded blocks aligned with the excavation flow are ejected most easily because they experience the least effective shear stress.

In this paper we present a study of Endurance Crater at Meridiani Planum on Mars, based primarily on observations acquired by the Opportunity rover. These observations present an uncommon chance to study the structure of a simple impact crater for several reasons. First, Endurance formed in horizontally-layered sedimentary rocks, where these layers can be easily traced on the crater walls to characterize the deformation. Second, Endurance is extremely fresh by terrestrial standards, and belongs to a size range (diameter $D = 150$ m) that is rarely so well preserved on Earth, where small craters are quickly eroded and buried. Third, Endurance formed in a target that is cut by conjugate-orthogonal joints whose azimuths can be easily measured and compared with the crater planform. These target materials are almost unique in crater studies because the fractures have a measurable width (unlike hairline fractures, and therefore unlike most tectonic joints on Earth and elsewhere on Mars). Fourth, because there are abundant orbiter images of Meridiani Planum, we have gained further insights from the surrounding population of small craters. The findings in this paper were reached by integrating the observations of instruments on three spacecraft: the Mars Global Surveyor (MGS), Mars Reconnaissance Orbiter (MRO), and Opportunity (MER-B).

This paper is organized as follows. In Section 2 we describe the stratigraphy and pattern of layering and faulting observed on the crater walls. This is used in Section 3 to construct a model of layering in 2-D radial cross-section through the crater walls. The cross-section models are then used to make a 3-D model of layering *within* the crater walls. This is done by adjusting the position of the flap hinge as a function of azimuth to match the pattern of layering *on the surface* of crater walls. The resulting 3-D flap hinge reflects the shape of the transient crater planform. In Section 4 we describe the relationship between conjugate fractures in the target rocks and the crater planform in the case of Endurance, Barringer, and Tswaing Craters. In Section 5 we present models of crater formation that illustrate how aligned fractures can influence the planform excavation flow, producing marked asymmetries in crater

Table 1
Glossary of terms and acronyms.

Term	Definition
3DLM	3-D Layer Model
DEM	Digital elevation model
MER	Mars Exploration Rover
MOC	Mars Orbiter Camera
MRO	Mars Reconnaissance Orbiter
RSM	Radial section model
PP1	Panorama Position 1 (see Fig. 4, part B)
PP2	Panorama Position 2 (see Fig. 4, part B)
Azimuthal position	Angular position around the crater in degrees clockwise from North
Incurvate ejecta	Pattern of layering in continuous ejecta shown in Fig. 18, associated with stellate crater growth
Lenticular-crescentic	Pattern of layering marked by lenses or smiles (crescents) interposed between corners of a polygonal impact crater that formed in a horizontally-layered target via stellate growth
Knurl	Prominence or concavity in the transient crater planform (see Fig. 17) associated with stellate growth
Stellate crater growth	Crater growth following Model C in Fig. 17, producing a transient crater whose planform is concave and cuspate

growth and the main structural features of Endurance and Barringer Craters. In Section 6 we compare Endurance to the well-known structural types of terrestrial craters. Finally, in Section 7 we discuss the implications of our structural model for understanding how Endurance and other Meridiani craters have been modified by wind-blown sand abrasion over long time scales. In Appendix A we present a detailed error analysis of estimates of bedding plane orientations. Some definitions of acronyms and terms used throughout this paper are supplied in Table 1.

2. Geological structure of Endurance Crater

The geology of the Opportunity landing site at Meridiani Planum has been described in detail elsewhere (e.g., Grotzinger et al., 2005; McLennan et al., 2005). Grant et al. (2006, 2008) studied the processes that have modified Endurance and nearby craters over long time scales. In this section we focus on the geological structure of Endurance Crater as determined by measurements of bedding plane orientations in the crater walls and the pattern of layer deformation and faulting caused by the impact. The main results of this section are: (a) maps of the strike and dip of bedding planes in Fig. 1 and reported in Appendix A; (b) the tracing of unit contacts and major faults in Fig. 2 (see also Fig. 3 without markings); and (c) the stratigraphic column shown in part C of Fig. 4. In what follows, we describe how these maps and models were generated as well as explain our assumptions and interpretations.

Throughout this work we refer to positions around the crater using an azimuth measured clockwise with respect to a line pointing North from the crater center (i.e., the "azimuthal position"). The crater center is the averaged center of circles fitted to four contour levels (separated by 4 m, spanning most of the crater's depth) of a digital elevation model (DEM) of the entire crater described below in Section 3. The center is marked in part B of Fig. 4 on a co-registered HiRISE image. Prominent corners in the crater planform have been labeled with the prefix "C" followed by the azimuthal position (Fig. 4).

Our analysis makes use of false-color Pancam panoramas acquired from two positions on the crater rim, and measurements derived from local DEMs of topography within ~10 m of the rover. The local DEMs were generated from short-baseline stereo image pairs acquired using the Navcam (20 cm baseline; Maki et al., 2003) and Pancam (30 cm baseline, red and blue filter pairs; Bell et al., 2003) cameras on Opportunity. Measurements of bedding plane strike and dip are derived entirely from these local DEMs, and were therefore acquired only along the rover traverse on the south crater wall, from azimuthal position 180–245°: i.e., slightly southeast of C249 to where ζ is labeled in part B of Fig. 4. The local DEMs used to measure structural strike and dip should not be confused with the whole-crater DEM described in Section 3, which is based on a combination of short- and wide-baseline observations. A detailed explanation of measurements of bedding plane orientations and associated error estimates are supplied in Appendix A.

2.1. Stratigraphic column

A stratigraphic model of the Endurance Crater walls is shown in part C of Fig. 4. The pre-impact surface, dividing the upright ("pre-impact") from the inverted ("overturned") strata occurs in a sand layer ("unit S") having at most several meters of apparent thickness (i.e., thickness measured on the crater wall, distinct from "true thickness"). This interpretation is based on three observations (see Fig. 5): (a) in many locations, the pattern of strata beneath unit S occurs in reverse order above this unit (i.e., in an inverted sense); (b) unit S has a smooth surface on the crater walls, unlike the rough sandy surface that occurs wherever sand covers rock at lower elevations on the wall; (c) the plains at Meridiani are covered with a mantle of sand that is in places up to 10 cm to 1 m thick (Soderblom et al., 2004, based on depths of small craters and troughs that intersect bedrock) and the crater's ejecta appear to rest partially on top of this sand at Endurance and other fresh craters in the vicinity. (Alternatively, unit S corresponds to a stratum of rock that is more susceptible to weathering and erosion, and that became a trap for sand.) An especially clear example of the upright and inverted strata is shown in Fig. 5. The stratigraphic model in part C of Fig. 4 reflects the true thickness of units only in the upright portion. The overturned units are assumed to have the same true thickness as their upright counterparts. In reality, the thickness of overturned strata decreases with distance from the crater rim (McGetchin et al., 1973), and inverted strata maintain coherence only near the hinge of the overturned flap.

Below unit S is a unit of light-toned rock (unit I in part C of Fig. 4) measuring just ≈25 cm in true thickness, which can be readily identified and traced in false-color Pancam images of the crater walls. Beneath this are two diagenetic horizons (i.e., which bound units II and III in part C of Fig. 4), below which the rocks are darker, and which have been interpreted as diagenetic fronts associated with a fluctuating water table (Grotzinger et al., 2005; Knoll et al., 2008). As discussed in Section 7, rocks belonging to the darker, upper portion of units II and III are more resistant to erosion, possibly because of significant recrystallization. (Evidence for cementation is visible in Microscopic Imager (MI) images, Herkenhoff et al., 2004, 2008; McEwen et al., 2005). The lower boundary of the dark upper bands in units II and III is somewhat variable and indistinct. A sporadically visible minor diagenetic horizon occurs near the base of unit III.

The rocks in units I–III exhibit mostly parallel bedding planes, with some low-angle cross-stratification ("sand-sheet facies"; Grotzinger et al., 2005). All of the strike and dip measurements reported in Appendix A and plotted in Fig. 1 were derived from rocks in these units only. The apparent thickness of units I and II were measured in multiple locations and combined with estimates of structural dip to obtain the true thicknesses shown in Fig. 4. The mean true thicknesses and standard deviations are: Sand (S): 1.11 ± 0.14 m; unit I: 0.26 ± 0.02 m; unit II: 0.92 ± 0.08 m. For unit III we have assumed the result reported in Grotzinger et al. (2005) of ~3 m.

We have not estimated the structural dip of the diagenetic horizons that separate units I–III because of (a) insufficient relief and definition on the scale of individual rocks and (b) sufficient relief only at the scale of the impact-related deformation (i.e., on the scale that strata are significantly warped and folded). Instead, we have measured the orientation of bedding planes in the rocks belonging to these units, always over a distance $\leqslant$1 m.

In drawing inferences about the impact-related deformation from Pancam images of the crater walls, we have assumed that these units were horizontal before the impact. Approximately horizontal diagenetic horizons similar to the ones bounding unit II and with similar separation also occur several kilometers to the south (Squyres et al., 2009). In drawing inferences about the impact-related deformation implied by the structural dip of bedding planes, we have assumed this dip was approximately zero in units I–III before the impact, as commonly observed on the plains for several kilometers to the south of Endurance. Moreover, in connecting these two sets of observations, we have assumed that the strike and dip of units I–III and of bedding planes within these units approximately coincide, as described in Grotzinger et al. (2005): i.e., horizontal bedding planes were deposited and lithified, and not rotated with respect to a fluctuating water table that later formed the diagenetic horizons. At the base of unit III is an erosional surface (called "Wellington" in Grotzinger et al. (2005)) that marks the upper

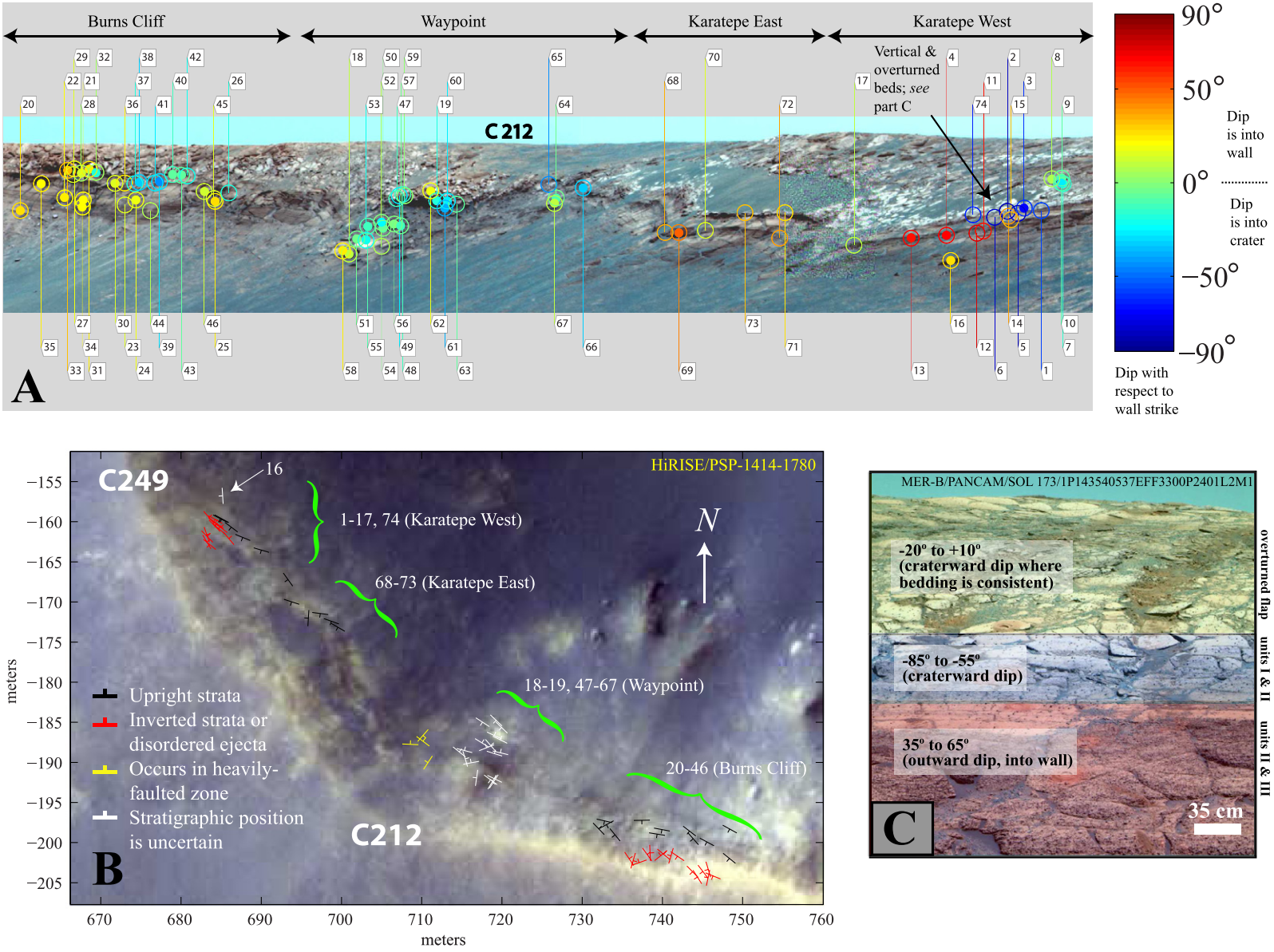

Fig. 1. (A) Mean structural dip of bedding planes measured from individual rocks, plotted on the Pancam panorama acquired at Panorama Position 1 (PP1). Shown are all dip estimates for which the 95% confidence interval is less than 20° ($\Delta\vartheta_+ + \Delta\vartheta_- < 20°$). Open circles are used where the fraction of inter-point deviation is less than one ($\xi < 1$). Solid circles are used where the look-plane proximity is greater than one ($\kappa > 1$). (These quantities have been defined in Appendix A, where the estimates of structural strike and dip are described in detail.) Here, the dip domain has been unfolded to [−90°,90°) with respect to a modal strike of ≈130°. Rocks have been assigned numeric labels, so that the estimates for each rock can be found in Tables 2–5. Note that rock 16 protrudes above the wall surface and is thought to be rotated and in float. This image is a subset of the mosaic shown in part D of Figs. 2 and 3. (B) Markers indicate the strike of bedding planes and dip direction of the rocks in part A, plotted on a HiRISE image of Endurance Crater. (C) Pancam false-color image (acquired sol 173) of Opportunity's tracks at "Karatepe West" (see parts A and B) after entering Endurance Crater. Marked are the approximate boundaries of the overturned flap, bedding that dips craterward, and bedding that dips into the crater walls at this location.

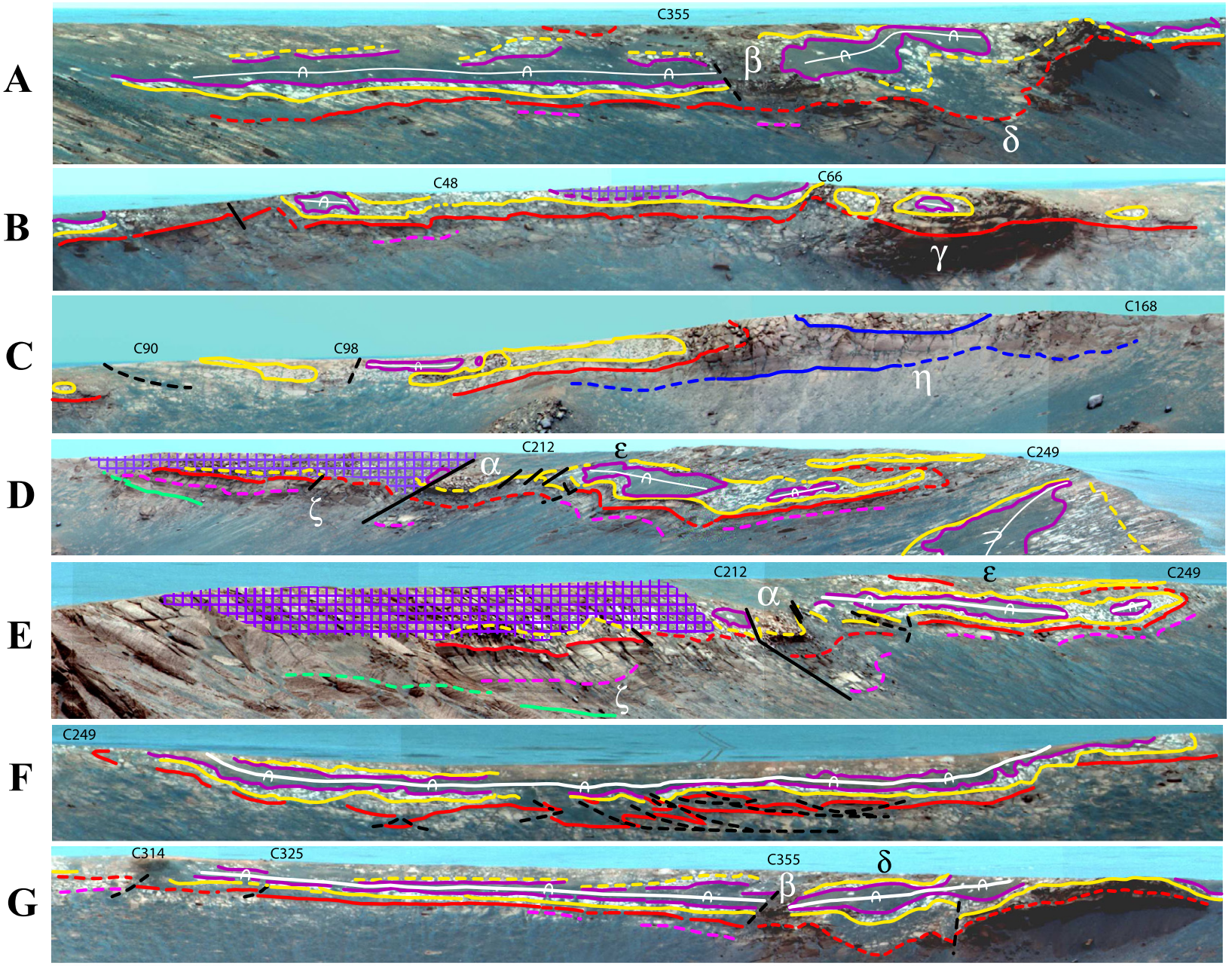

Fig. 2. Delineation of unit contacts and structural features in false-color Pancam panoramas from Panorama Position 1 (PP1, frames A–D, acquired on sols 96 and 97: sequence IDs 2291–2294 and filters L257) and Panorama Position 2 (PP2, frames E–G, acquired on sols 117 through 123: sequence IDs 2260–2267 and 2298–2299, and filters L257). See Fig. 4 for a symbol and color legend.

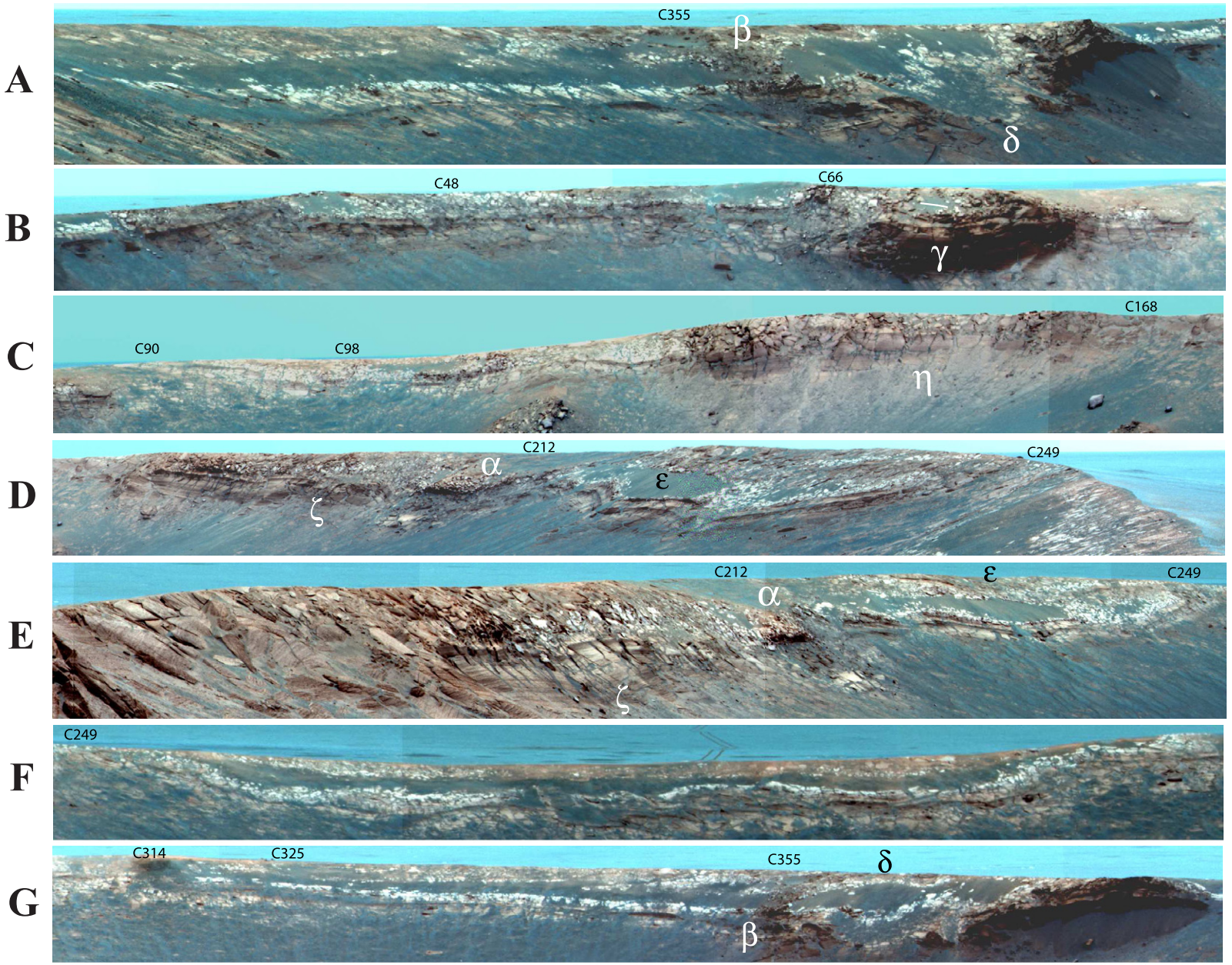

Fig. 3. False-color Pancam panoramas from Panorama Position 1 (PP1, frames A–D, acquired on sols 96 and 97: sequence IDs 2291–2294 and filters L257) and Panorama Position 2 (PP2, frames E–G, acquired on sols 117 through 123: sequence IDs 2260–2267 and 2298–2299, and filters L257). Absent are the markings in Fig. 2 for the purpose of comparison. (For interpretation of the references to color in this figure legend, the reader is referred to the web version of this article.)

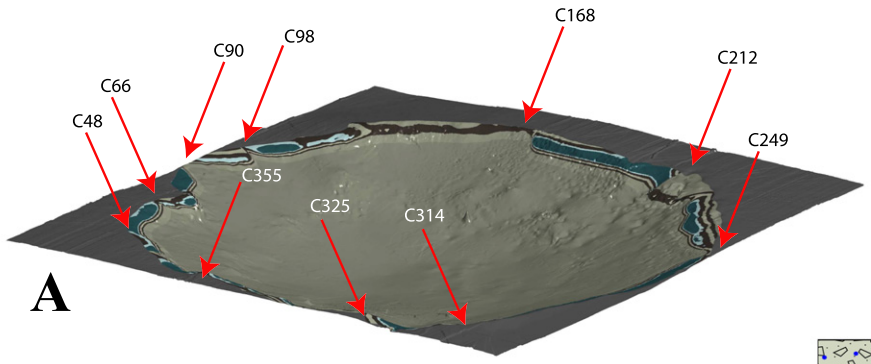

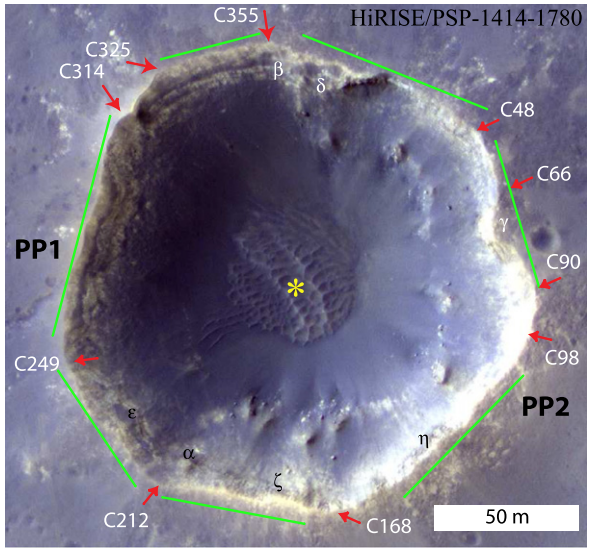

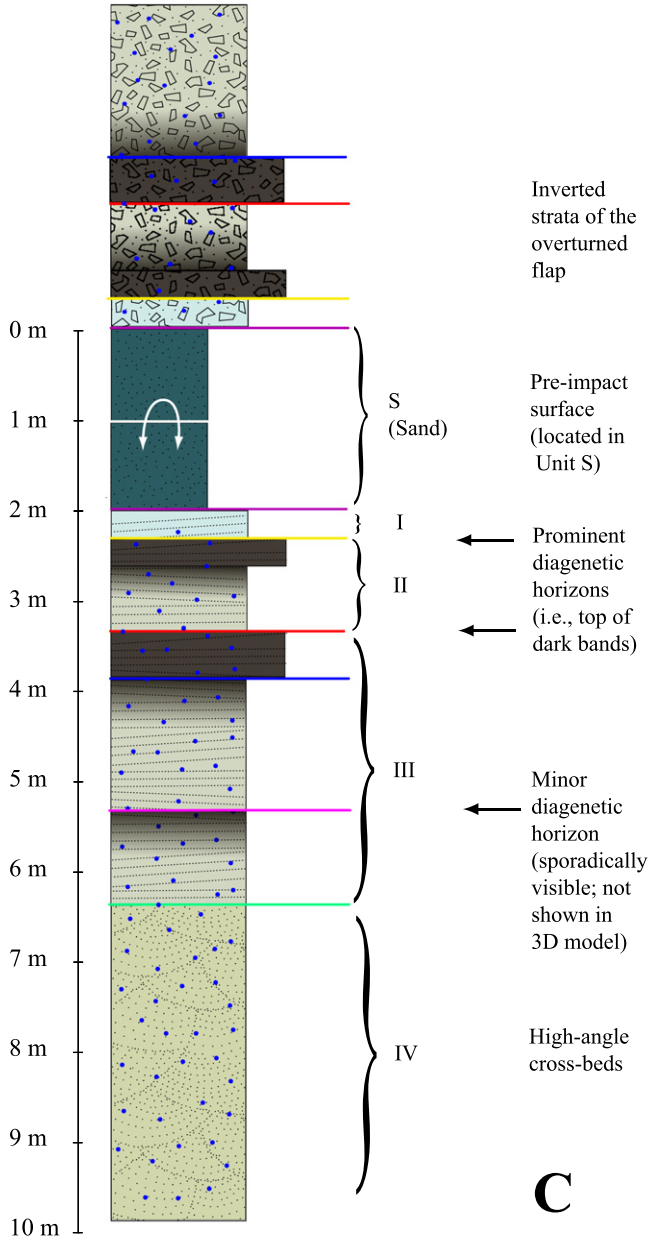

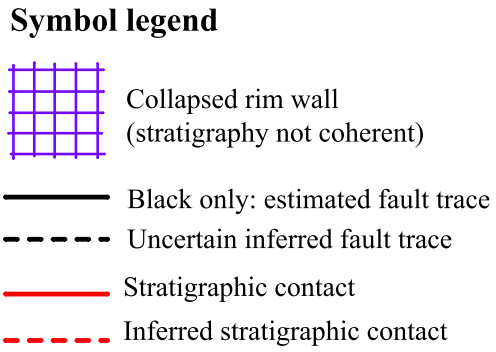

Fig. 4. Visual aids and models to assist with the interpretation of Figs. 2 and 3. (A) 3-D Layer Model (3DLM) cut-away by the global crater DEM (i.e., oblique view of the model in Fig. 9). (B) HiRISE image of Endurance Crater, with corners labeled by azimuthal position from central yellow star (e.g., C249 is the corner located at 249° clockwise from North). Features labeled in Fig. 2 are marked with Greek letters. (C) Stratigraphic model of the Endurance Crater wall (near the flap hinge), with color-coding of contacts applied in Fig. 2. The blue dots signify the presence of ~5 mm scale hematitic concretions. A legend of symbols and boundaries also used in Fig. 2 is shown at lower left.

boundary of an aeolian unit ("unit IV" in part C of Fig. 4) with high-angle cross-beds like those observed kilometers to the south in the walls of Victoria Crater (Squyres et al., 2009; Hayes et al., 2010; Edgar et al., in preparation). We did not acquire measurements of strike and dip in unit IV, and avoided low-angle cross-beds in units I–III as far as possible. Units I and II together correspond to the

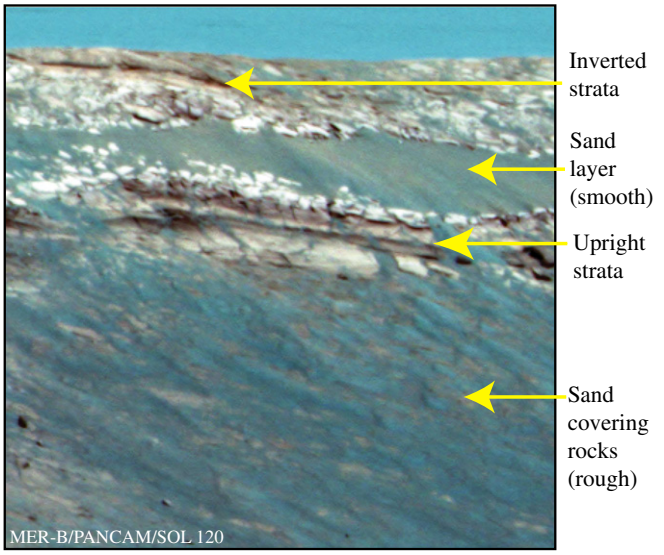

Fig. 5. A false-color Opportunity Pancam image of "Karatepe East" taken from Panorama Position 2 (PP2). The inverted stratigraphy of the overturned flap is clearly visible, as well as a marked contrast between the unit S "sand layer" (smooth, in which the flap hinge resides), and rocks lower on the wall covered by sand.

"Upper Unit" in Grotzinger et al. (2005), while unit III corresponds to their "Middle Unit," and unit IV to their "Lower Unit."

In impact and explosion cratering experiments, layers that are horizontal prior to impact are used as fiducial markings to illuminate the impact-related flow and deformation. For convenience, throughout this text we will sometimes refer informally to units I–III and the dark diagenetic bands at the tops of units II and III as "layers" or "layering."

2.2. Tracing unit contacts

In parts A–D of Fig. 2 we have traced the unit contacts in a panorama assembled from Pancam images acquired at "Panorama Position 1" or PP1 on the west rim (i.e., azimuthal position ≈275°, shown in part B of Fig. 4). This was repeated in parts E–G for a panorama acquired from "Panorama Position 2" or PP2 on the southeast rim (i.e., azimuthal position ∼100°). The apparent thickness of the sand layer (unit S) varies markedly, pinching-out altogether in some locations. For long stretches of the southeast wall, the sand unit is completely absent (Fig. 2, part C). Of special interest is that layering occurs in the pattern of an "open smile" or "lens" between some corners of the crater, as shown in Figs. 2 and 3: e.g., between C212 and C249 (labeled ϵ) in parts D and E; adjacent to C355 (labeled δ) in parts A and G; as well as the entire west wall between C249 and C314 in part F. The possible origins of this pattern will be examined in Section 5.

2.3. Dip and strike of bedding planes

The structural dip of bedding planes has been plotted in part A of Fig. 1 and strike in part B. Where Opportunity entered the crater (called "Karatepe West" in Fig. 1) we identify a transition from beds dipping steeply into the crater wall at lower elevations (red markers) to vertical and then overturned bedding higher on the rim wall (blue markers, negative dip angles). We identify this transition as a hallmark of the flap hinge inside the crater wall, which has been recognized in few terrestrial impact craters, most famously at Barringer Crater by Shoemaker (1960). Its presence marks an important constraint for our structural model at this location, where the sand layer is enclosed by units I and II. Measurements farther east at Karatepe as well as Burns Cliff indicate that beds below the sand layer are dipping away from the crater center. At the "Waypoint" location, bedding has a gentle outward dip or a slight craterward dip. This latter result may suggest the rotation of a large block associated with post-excavation slumping, or as we suggest in Section 3, a large tear fault in this corner of the crater planform. In part B of Fig. 1 we have plotted the mean strike of the rocks from part A. The strike of bedding planes in the upright strata conform roughly to the local wall strike, as expected for concentric uplift that everywhere decreases radially outward. Strike and dip of bedding planes were only measured along the rover's traverse, over roughly one-fifth of the crater's circumference.

2.4. Faulting

In addition to marking the unit boundaries in Fig. 2, we have drawn the locations of sharp discontinuities that cross single or multiple contacts and which are interpreted as faults. There is nowhere sufficient relief along a fault to estimate its orientation. In many cases even the trace of a fault on the crater wall is highly uncertain (indicated by a black dashed line in Fig. 2) where its presence is inferred from a diffuse discontinuity. Many faults appear to occur near corners of the crater planform. Major faults near corner C212 (see part A of Fig. 1 and parts D and E of Fig. 2) are indicated by a sharp discontinuity in layering and change of structural dip. The change in bedding orientation indicates a significant scissors-like displacement (i.e., a transition from dips of ∼30° into the crater wall to dips ∼15° craterward) that may reflect the presence of one or more tear faults like those found in the corners of Barringer Crater (Shoemaker, 1960; Roddy, 1978). The meters-wide and apparently rotated block at corner C212 in the southwest (labeled α) resembles a structure that occurs at corner C355 in the north wall (in parts A and G of Fig. 2, labeled β). Both structures may correspond to fault-bounded sectors of the crater wall over which bedding cannot be traced because of dislocation, rotation, or layer mixing. The significance of these and other corner-associated fault zones is discussed in Section 5.

By tracing the upper and lower contacts of I and II in the west (part F of Fig. 2), we find a series of faults imbricating the crater walls, whose orientations also cannot be established. These may correspond to the shallow outward-dipping rotated faults or the steeper inward-dipping over-thrusts described at many terrestrial impact craters (e.g., Shoemaker and Eggleton, 1961; Kring, 2007; Maloof et al., 2009) and associated with uplift of the crater wall in the final stage of excavation. Of these two, the extensive imbrication may favor the over-thrust interpretation. These structures are concentrated in the west wall, and similar faults rarely occur elsewhere. The west wall has the shallowest slope and the lowest rim and is therefore most heavily eroded (Grant et al., 2006). That is, imbrication of this kind may tend to occur deeper in the crater walls, and is possibly covered with sand where such fault systems intersect the less-eroded walls at lower elevations.

3. Three-Dimensional Layer Model

Judging by its present depth–diameter ratio (0.14) and estimates of the extent of infilling and back-wasting of the crater walls and relative isolation, Endurance is a primary impact crater (Grant et al., 2006). As mentioned in Section 1, the rim walls of hypervelocity craters commonly exhibit a circumferential, overturned synclinal fold whose upper limb is called the "overturned flap." The axis of this fold (the "flap hinge") forms before the onset of slumping (Melosh, 1989), and therefore reflects the planform shape of

the transient crater. A primary goal of this section is to estimate the 3-D path of the flap hinge (the "hinge line") and in this way estimate the transient crater planform. As we describe in Section 5, this result will be the source of several new insights about the formation of small craters, and will show to what extent the present shape of Endurance was mainly determined in the excavation stage or the modification stage.

3.1. Model of radial cross-sections

Using the stratigraphic column from the previous section we construct radial cross-sections through the crater walls, hereafter known as Radial Section Models (RSM). These models are partly based on the radial cross-sections drawn in studies of Barringer Crater (e.g., Shoemaker, 1960; Shoemaker and Eggleton, 1961) and approximately reproduced in laboratory experiments and explosion craters (e.g., Stoeffler et al., 1975; Carlson and Jones, 1965). Later in this section, these models are used to reproduce the pattern of layering and structural dip in the crater walls by adjusting only the hinge position in 3-D. We obtain the 3-D path of the flap hinge in this way, and thereby estimate the transient crater planform.

We experimented with many shapes for the radial cross-section. From these, two were chosen because they can match the pattern of layering and structural dip in the most locations. These model cross-sections (RSM1 and RSM2) are shown in Fig. 6. The expected true thickness variation of the inverted strata is poorly constrained by previous field studies and laboratory experiments. This matters little because we will not attempt to match model apparent thicknesses with observed apparent thicknesses in the overturned flap, since the inverted stratigraphy is not well preserved

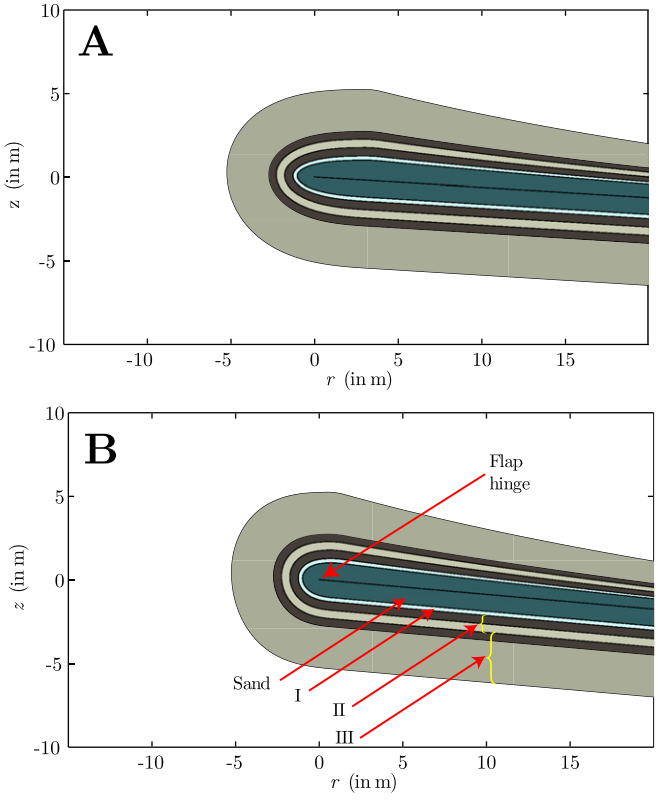

Fig. 6. (A) Radial section model 1 (RSM1) and (B) radial section model 2 (RSM2), with the flap hinge located at the origin. Important structures and stratigraphic units have been labeled as in part C of Fig. 4. The units have been color-coded with colors sampled from the false-color panoramas in Figs. 2 and 3.

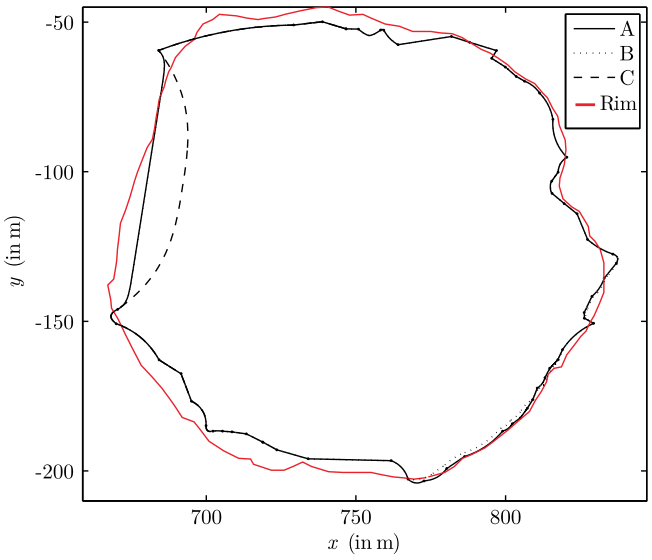

Fig. 7. Planform of hinge line A and alternatives B and C in the 3-D Layer Model (3DLM). (A) Radial section model 1 (RSM1); (B) RSM2 (in the southeast corner only); (C) RSM1 (everywhere the same except the west wall). The hinge line is not expected to be accurate in the northwest corner, where the crater DEM is not reliable. The crater rim (extracted from the global DEM) is plotted in red. The hinge exhibits marked concavities but otherwise closely resembles the present-day crater planform. It is also clear that the southeast and northeast walls are the least eroded. (For interpretation of the references to color in this figure legend, the reader is referred to the web version of this article.)

in all locations. For completeness, we have assumed that the true thickness of inverted strata decreases as $\sim r^{-3}$, consistent with McGetchin et al. (1973) for the radial decrease in continuous ejecta thickness.

In generating RSM1 and RSM2, we have approximated the radial stratigraphic uplift as a straight line oriented at just 4° with respect to horizontal. This is based on estimates of the elevation of unit I at the Karatepe ingress location on the south wall, the elevation change measured along the traverse from Eagle crater (at a distance of several crater diameters) to the west rim (Arvidson et al., 2004), and the assumption that stratigraphic uplift persists to distance $\sim 0.6R$ beyond the crater radius R (Melosh, 1989; Roddy et al., 1975). At Barringer Crater ($D \approx 1.2$ km) the uplift angle exceeds 30° near the rim (Kring, 2007) and the pre-impact surface elevation decreases exponentially with distance from the rim (Roddy et al., 1975; Pilon et al., 1991). However, in laboratory experiments and smaller explosion craters ($D \leqslant 100$ m) formed in low-strength targets, the uplift is approximately linear and the angle of uplift is commonly less than 10° (Gault et al., 1968; Carlson and Jones, 1965). As discussed later in this section, the uplift angle plays little role in our structural model because, in most locations, the walls of Endurance have not been eroded far enough to expose this part of the RSM. While the cross-sectional shape varies from one crater to the next (as well as within the same crater), trying the whole range of possibilities for small craters like Endurance would not affect the main result of our analysis, as discussed later in this section.

As mentioned, we experimented with many shape models for the fold shown in Fig. 6. Of these, RSM1 can be matched to the pattern of apparent layer thickness and structural dip in the most locations. The fold in this model is markedly more pointed or flattened than is commonly shown in the classic cross-sections of Barringer Crater. RSM2 is a better match to the layering pattern on the southeast wall. As shown later in this section, the difference between these two models has a negligible consequence for the derived 3-D path of the flap hinge. In both model cross-sections,

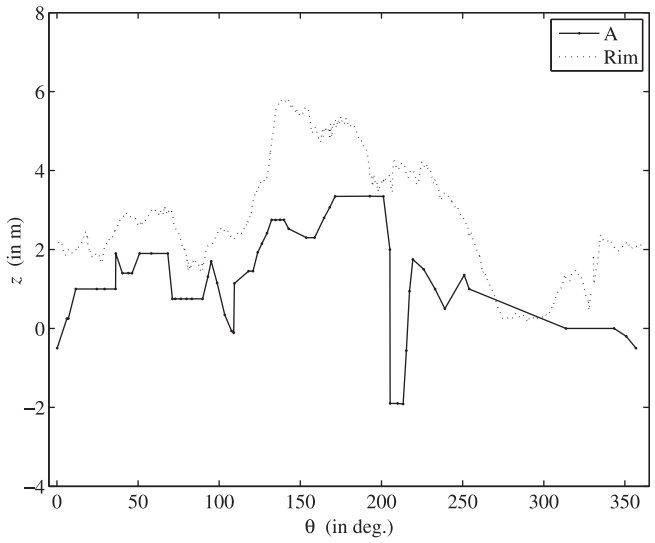

Fig. 8. Topography of the rim crest (dotted line) and flap hinge A (solid line) of the 3DLM, as a function of azimuthal position (i.e., in degrees clockwise from North). The minimum at ≈205° corresponds to the fault-bounded structure labeled α in Fig. 2, which may be a rotated block. The relief is roughly 6 m along each curve; the θ-axis spans the entire crater circumference, or about 500 m.

the true thickness of units I–III is the same as in our stratigraphic column (Fig. 4, part C) at the elevation of the flap hinge, as well as directly below the hinge. This is not exactly consistent with observations made in previous field studies and laboratory experiments, where some amount of bulking (expansion) of upturned layers has been noted (e.g., Regan and Hinze, 1975). In the absence of good estimates of the expected change in volume with position around the fold, we have assumed that layer thicknesses are consistent with their horizontal (undeformed) counterparts. Bulking may already contribute to thickness estimates in our stratigraphic column, in which case it does not make sense to compensate for this effect.

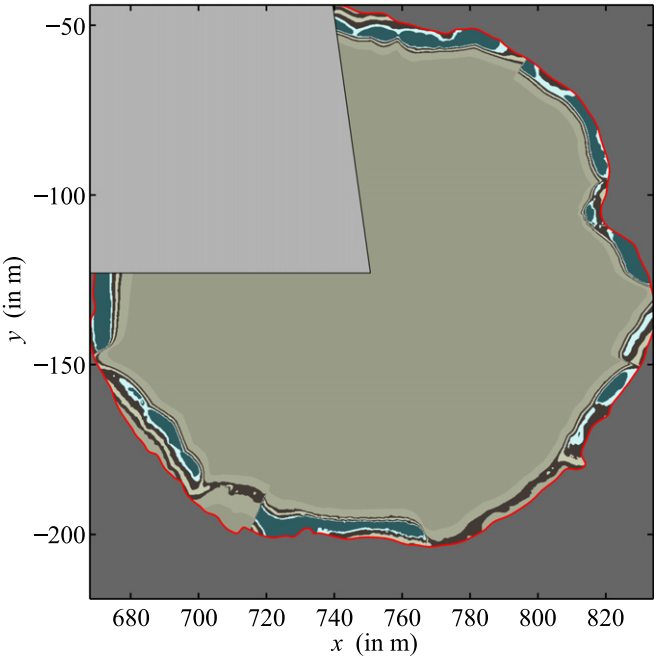

Fig. 9. Plan view of the 3-D Layer Model for hinge line A and RSM1 (defined in Figs. 6–8). The northwest corner has been occluded because the DEM in this region is not reliable. Wherever the sand layer (dark green) is not exposed, the hinge is preserved inside the crater wall; this is commonly the case near corners of the crater. The red line is a trace of the present-day rim, derived from the crater DEM. (For interpretation of the references to color in this figure legend, the reader is referred to the web version of this article.)

3.2. 3-D model

The Three-Dimensional Layer Model (3DLM) is built from two ingredients: (a) the radial section model (RSM1 or RSM2) and (b) the 3-D hinge line. The hinge line is the circumferential fold-axis of the overturned flap, defined in cylindrical coordinates (r,θ,z), where θ refers to azimuthal position. A major simplifying assumption of the 3DLM is that only the position of the hinge in the (r,z) plane changes with the cross-section azimuth θ. That is, the shape of the fold and the uplift angle do not change with azimuth. This is a significant simplification, and the resulting error in the estimated position of the hinge will increase with distance from the actual hinge. As shown later in this section, the difference between RSM1 and RSM2 accounts for a negligible difference in the hinge line. However, because of this uncertainty, we do not expect the estimated hinge line to be highly accurate. The purpose of this exercise is not to estimate the hinge line with great precision, so much as reveal large-scale features of its planform indicated by the pattern of layering in the crater walls. Our goal is to identify where major inflections occur, where the hinge is preserved, as

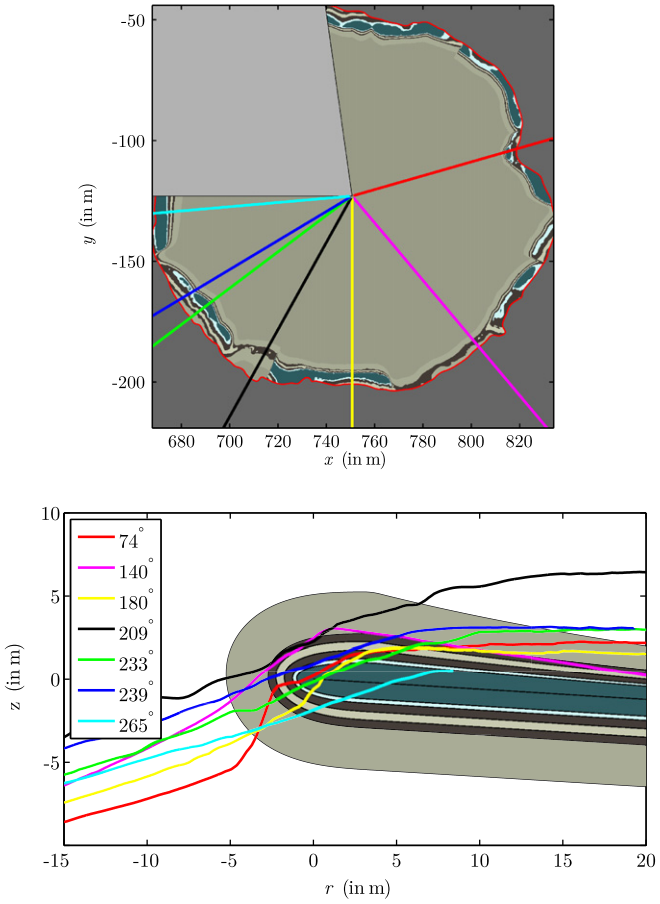

Fig. 10. Radial section model 1 (RSM1) with radial topographic profiles of the crater DEM (i.e., derived from the 3DLM with hinge line A, shown above). For convenience, each profile is plotted with respect to the flap hinge so that many can be plotted on the RSM. That is, the coordinate frame is centered on the hinge, so that profiles can be compared to the RSM but not to each other.

well as where the hinge is plunging into or emerging out of the crater walls, and to gain a sense of the overall shape.

3.3. Estimation of the hinge line

We use a global DEM of Endurance Crater at 30 cm resolution (Li et al., 2007) to cut-away the 3DLM and reveal the pattern of layering on the crater walls. The software used to perform the visualization steps described in this section were written using the MatLab numerical programming language. The global crater DEM was assembled from short-baseline Pancam panoramas acquired at PP1 and PP2 as well as a wide-baseline (5 m) panorama inside the crater (Li et al., 2007). Because image coverage was not sufficient in the northwest corner of Endurance, the DEM is unreliable in this area and has been excluded.

The hinge line is obtained through an iterative process. The initial guess of the hinge line is a piecewise curve assembled from straight line segments and circular arcs. Cut-aways of the model along hinge segments that deflect outward or center-ward produce distinctive patterns that can be used that inform the initial guess, as shown in Section 5. Then, the 3DLM is cut-away by the DEM and the pattern of layering is compared to the PP1 and PP2 panoramas (draped on the DEM), and model dips are compared to the pattern of true structural dips where these were measured on the south wall. The hinge line is then manually adjusted and the process is repeated until there is quantitative agreement with structural dips (see below, this section), and qualitative agreement between the modeled and observed pattern of layering.

The resulting hinge line is shown in Fig. 7 (plan view) and Fig. 8 (in z vs. θ). Hinge A was obtained with RSM1 (Fig. 6, part A) around the entire crater, and hinge B is used for an alternative interpretation of the southeast wall, using RSM2. Although different RSMs were used, the difference between the curves in each case is negligible. Hinge C with RSM1 illustrates the uncertainty regarding the hinge position with respect to the west wall, where the low rim elevation and wall slope and thin sand layer suggest the wall surface lies far behind the hinge position (the hinge is not preserved), although it is impossible to estimate by what distance.

Significant discontinuities in the plot of hinge elevation as a function of azimuthal position (Fig. 8) may correspond to major faults, rotated blocks, or slumps. Possible origins of these features are discussed in Section 5. For now we consider two interpretations of the largest example, located at azimuthal position ≈205° and labeled α in Fig. 2 (i.e., in corner C212). Because the bedding in this location dips predominantly craterward (Fig. 1) the only possible match to the RSM is achieved by sharply dropping the hinge downward several meters. According to the 3DLM, the beds dipping craterward in this location occur on the leading edge of the overturned flap, in the inverted strata. The contacts drawn in Fig. 2 suggest an alternative interpretation: i.e., upright units I–III have been rotated craterward in a faulted block at α. Our interpretation of the structure labeled δ in the north wall is also uncertain (parts A and G of Fig. 2). The contacts drawn in Fig. 2 can be reconciled with RSM1 only for unit S (sand layer) and I, but not obviously also unit II. One difficulty is that sand may be covering the contact between units II and III at this location.

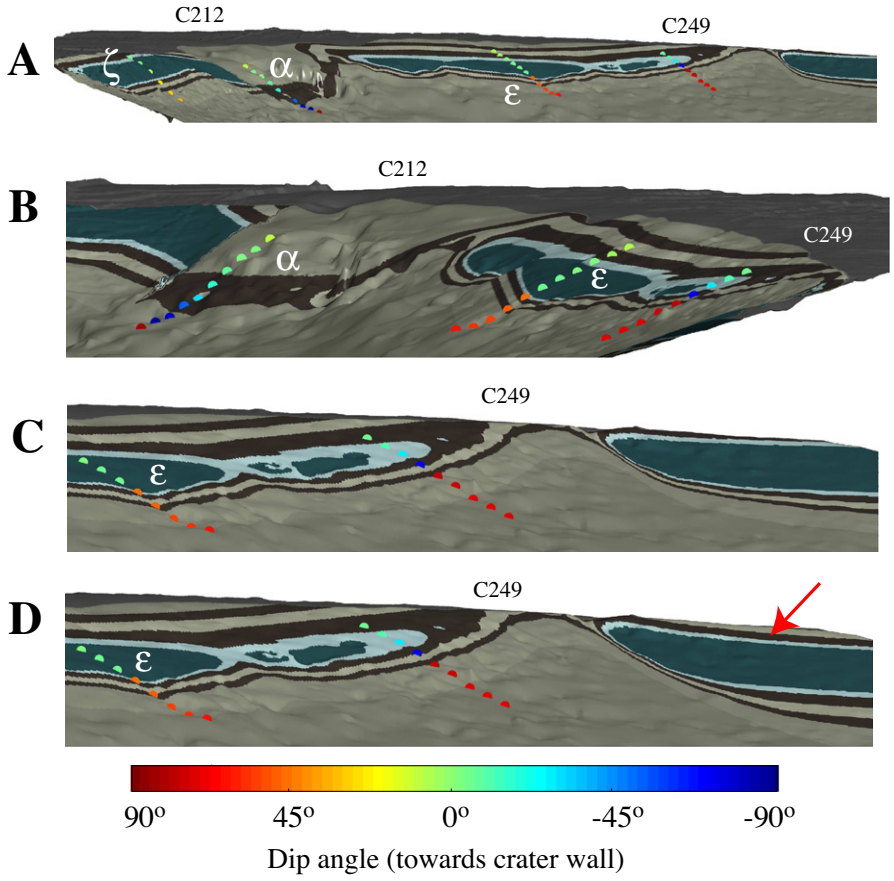

Fig. 11. (A)–(C) 3-D Layer Model (3DLM) of exposed layering and structural dip in key locations along the south wall (cf. Fig. 1, where measured dips are plotted on the south wall). This pattern is produced by RSM1 and hinge line A in Fig. 7. Corner positions and notable structures (Greek symbols) are also labeled for ease of comparison (cf. Fig. 2). Note that Burns Cliff (ζ) appears at the far left in part A. Dip is reported with respect to a reference strike of ≈130° so that negative values indicate craterward dip. (D) 3DLM pattern produced by hinge C and RSM1 in Fig. 7, which alters only the west wall at right (red arrow). (For interpretation of the references to color in this figure legend, the reader is referred to the web version of this article.)

The pattern of layering on the crater walls produced by RSM1 and hinge line A (Fig. 7) is shown in plan view in Fig. 9 and from an oblique view in part A of Fig. 4. Example cross-sections (with topographic profiles) are shown in Fig. 10. Detailed 3-D views of selected portions of the upper wall are shown in Fig. 11 for the southwest (RSM1 and hinges A and C), Fig. 12 for the east wall, and Fig. 13 for the remaining portions (RSM1 and hinge line A for the north and southeast walls, and RSM2 and hinge line B also for the southeast wall). An example cross-section and topographic profiles are plotted in Fig. 14 for an alternative 3DLM of the southeast wall constructed from RSM2 and hinge line B.

Model dip angles have been plotted in Fig. 11 for comparison with measurements along the south and southwest walls (Fig. 1). At Karatepe West, modeled and measured dips are mostly crater-ward and shallow ($\leqslant 20°$) in unit I, steepening to 85° in unit II, remaining steep (>50°) but dipping into the wall in unit III. As remarked earlier, this pattern is a hallmark of the flap hinge. At Karatepe East, the model was constrained by the most confident dip measurement of $\approx 45°$ into the crater wall. At Burns Cliff, the upright strata dip into the wall at $\approx 20°$. As mentioned earlier, the Waypoint location (α in Fig. 2) cannot be reconciled directly with the model, where dip appears to shallow and change orientation downslope. Also at this position, measured dips in the dark band are shallower and roughly constant over a larger area than occurs in the model. Alternative interpretations for this structure were described above.

The shape of the hinge line in Fig. 7 is partially concave. That is, the hinge is made up of bow-shaped segments that sometimes

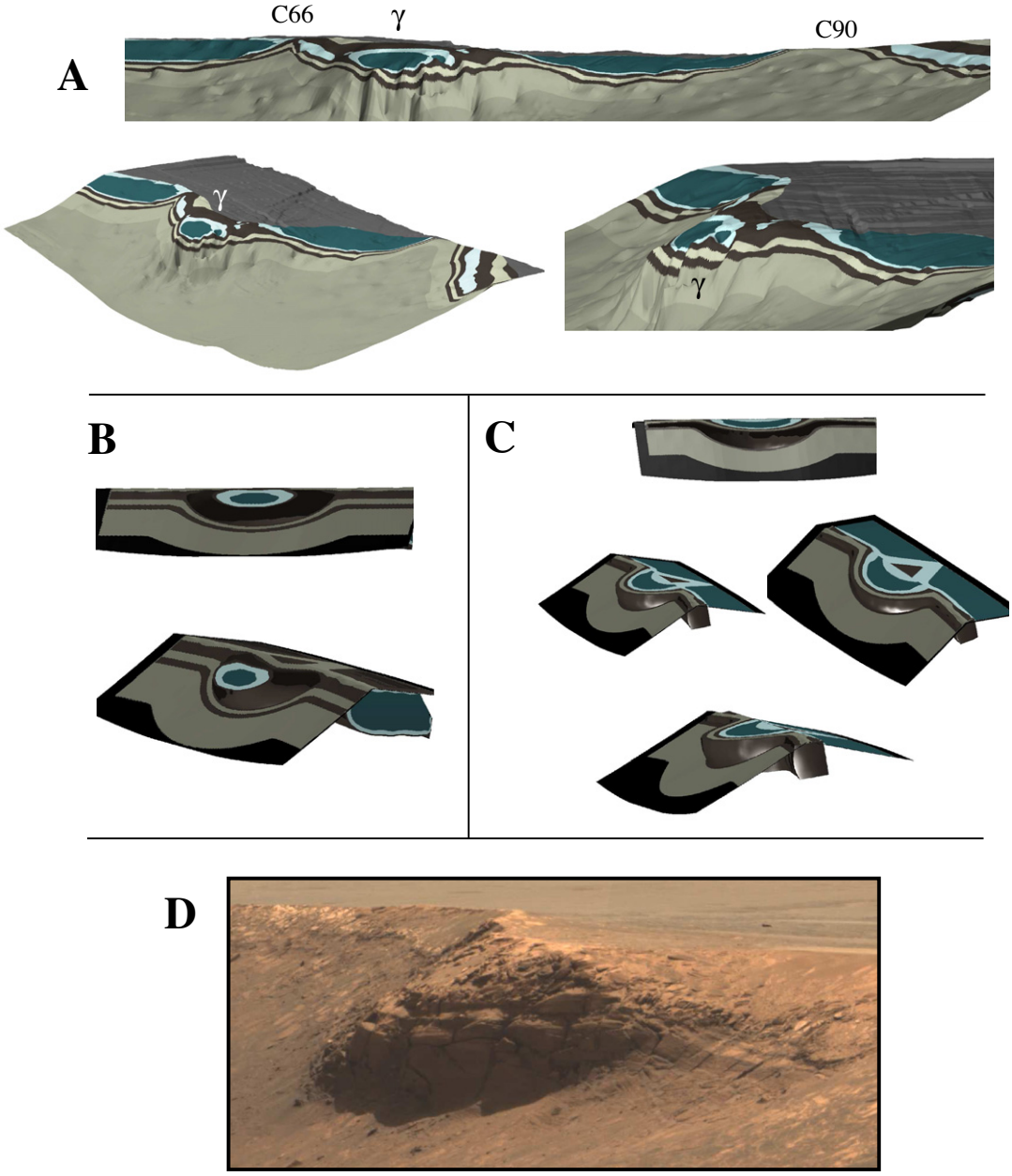

Fig. 12. (A) 3-D Layer Model (3DLM) of exposed layering on the east wall of Endurance Crater, including the γ knurl (see Section 5). This pattern is produced by RSM1 in Fig. 6 and hinge line A in Fig. 7. Corner positions have been labeled for ease of comparison (cf. Fig. 2, part B). Alternative models of the γ knurl (depicted in (D)) are shown in (B) and (C), where the dark bands in units II and III project from the surface. (A hybrid of these interpretations is presented in part B of Fig. 2 for the south flank of the γ knurl.) (D) The γ knurl shown in a true-color Pancam image acquired on sol 122 with sequence ID 2262. (For interpretation of the references to color in this figure legend, the reader is referred to the web version of this article.)

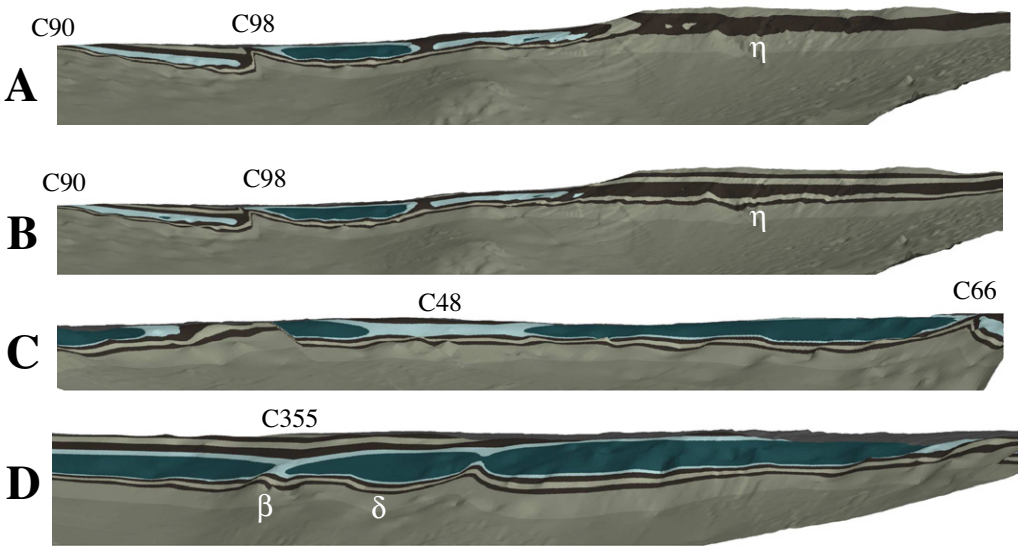

Fig. 13. Three-Dimensional Layer Model (3DLM) of exposed layering on (A) the southeast wall of Endurance Crater with hinge line A and RSM1; (B) the same section with hinge line B and RSM2 (cf. Fig. 2, part C); (C) northeast wall (cf. Fig. 2, part B) and (D) north wall (hinge line A, RSM1). Corner positions and notable structures (Greek symbols) are labeled for comparison with Fig. 2.

deflect into the crater. These concavities tend to occur between corners of the crater (cf. part B of Fig. 4) and prominent cusps tend to coincide with corners. In Fig. 9, the flap hinge is preserved (i.e., it is inside the walls) wherever the sand layer is not exposed, which happens in several corners. As mentioned earlier, the hinge planform reflects the transient crater planform: i.e., the plan-view shape of the transient cavity that formed before slumping destroyed a portion of the upper walls. In the following sections we will consider how a transient crater that is concave in plan view might have formed, as well as reflect on the similarity in shape between the transient and present-day planforms.

4. Relating target fractures to the crater planform

The bedrock at the Opportunity landing site is host to at least three kinds of fractures: (a) fractures formed by previous impacts; (b) small-scale polygonal shrinkage fractures (<1 m in length, McLennan et al., 2005) with random orientations; and (c) large-scale fractures (>1 m in length, 5–20 cm in width) that exhibit alignments in two mutually orthogonal directions. The nature of this fracture system was discovered during Opportunity's southward traverse toward Victoria crater where the plains bedrock is exposed in patches (part C of Fig. 15). In the vicinity of Endurance Crater, the plains are covered with sand, so that only the longest and widest fractures are expressed as trough-like depressions (parts A and B of Fig. 15) where sand has drained into the underlying fractures. Conjugate sets of wide fractures are highly unusual. On the Earth, conjugate fractures usually form as a consequence of tectonic stresses and have hairline widths. Conjugate tension fractures with a measurable width may form as a result of tension along mutually orthogonal directions at different times, or by dissolution or shrinkage in materials already fractured by tectonic stresses. Whatever the formation mechanism, a target having wide conjugate fractures is an extreme case of material strength anisotropy, and the consequences for cratering have been rarely observed. The other well-known example is Barringer Crater, where dissolution has widened prominent orthogonal joints in the Kaibab member (Roddy, 1978). Barringer and Endurance Craters bear many marked similarities in structure, as described in Section 5.

As mentioned in the introduction, it was long ago suggested that excavation is more efficient in the direction of pre-existing

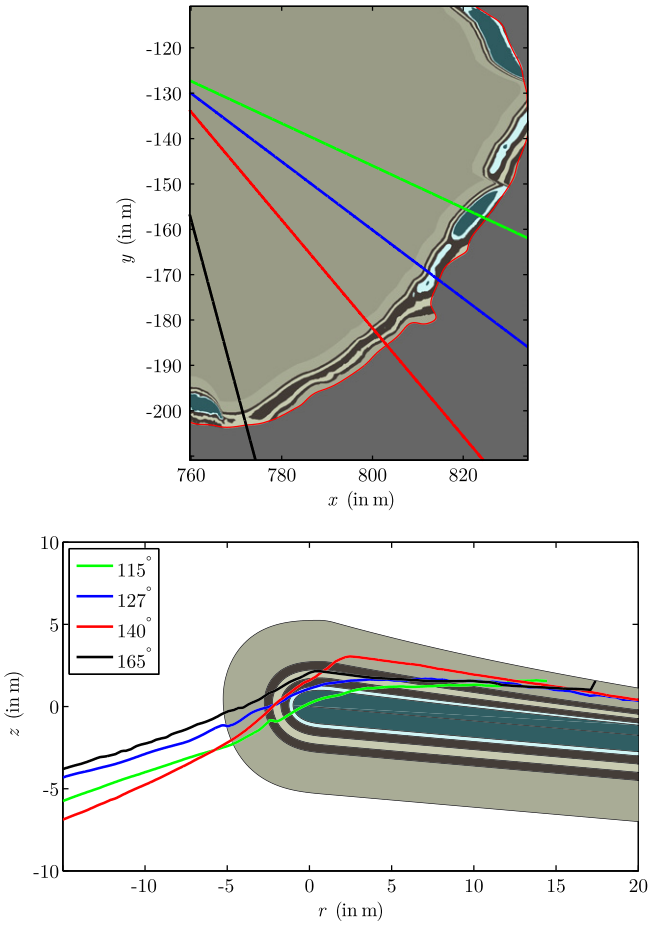

Fig. 14. Radial section model 2 (RSM2) with select radial topographic profiles of the Endurance DEM used to construct an alternative model for the southeast wall (see Fig. 13). For convenience, each profile is plotted with respect to the flap hinge so that many can be plotted on the RSM. That is, the coordinate frame is centered on the hinge for each case, so that profiles can be compared to the RSM but not to each other.

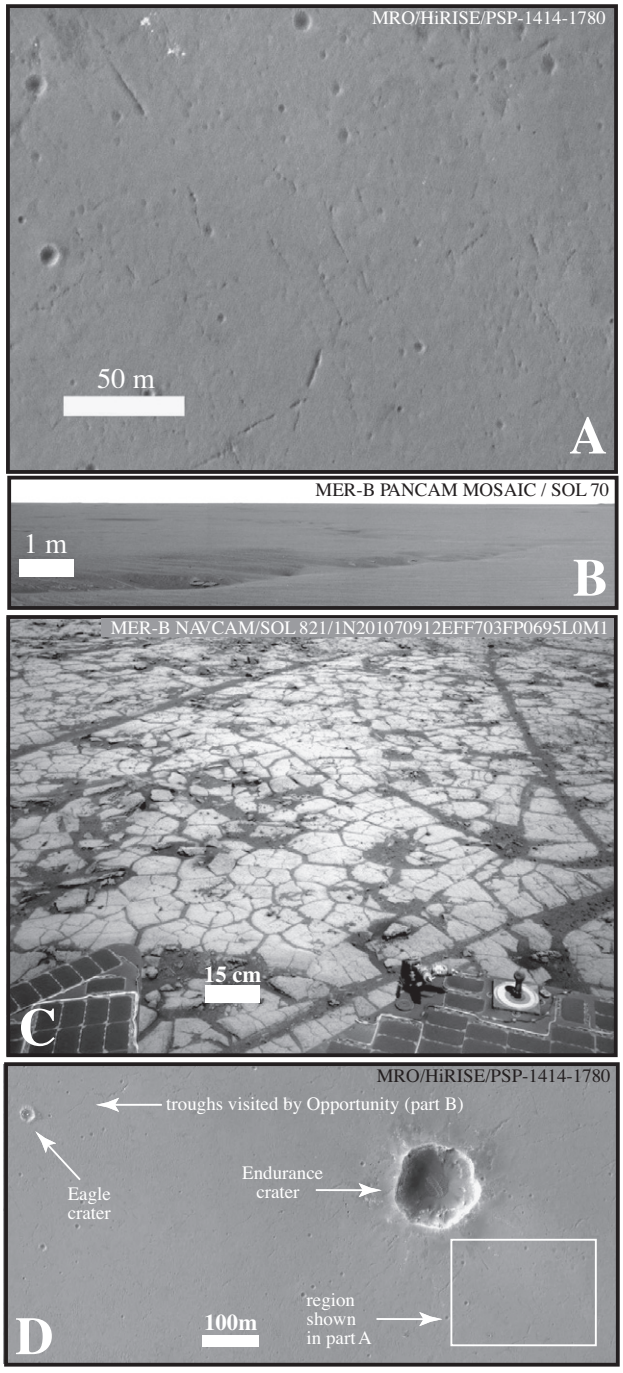

Fig. 15. Troughs formed in sands above fractures in underlying sandstones at Meridiani Planum as seen in (A) MRO/HiRISE and (B) Opportunity/Pancam images. (C) An exposed patch of plains bedrock with several long (>1 m) fractures that exhibit alignments over a broad area, as well as many smaller, randomly-oriented polygonal fractures (<1 m length). (D) A HiRISE image for context, showing the locations of Endurance Crater and the images in parts A and B. Opportunity landed in Eagle Crater at the extreme left.

planes of weakness. This explanation was famously invoked to account for the roughly square shape of Barringer Crater, where diagonals of the square planform align with major joint sets in the surrounding bedrock (Shoemaker, 1960; Roddy, 1978). In Fig. 16 we have made a similar comparison for Endurance Crater, by plotting a length-weighted histogram of the azimuths of linear troughs located within three crater radii of the rim of Endurance as measured in MRO-HiRISE images. (A cropped image of each trough was rotated through nine angles spanning 45° (i.e., 6°,12°,...,45°); we recorded the mean azimuth of straight lines drawn manually on these images, in order to preclude biases introduced by pixelation.) The distribution clearly shows a pair of approximately orthogonal modes at roughly −35° (or at 325°, equivalently) and 50° from North. But since Endurance is not obviously square-shaped, we have compared this distribution with two measures of the square component or "quadrature" of the rim-crest outline traced from the HiRISE image in part B of Fig. 4. The first is the "azimuthal diameter" ($D(\theta)$): the diameter as a function of azimuth, measured through the center of the modern-day planform (i.e., the center of a circle fitted to the crater's plan-view outline), and expressed as a fraction of the maximum deviation of diameter. The azimuthal diameter is found to have two peaks, one of which exactly matches the modal azimuth at 50° (the other peak is offset from the other modal azimuth by ∼10°). We have also plotted the phase of the fourth Fourier harmonic of the crater planform (computed as in Eppler et al. (1977)), whose peaks are perfectly aligned with the modal azimuth at −35° (the other is offset by ∼10°; recall that peaks of the azimuth distribution are not exactly orthogonal). The close correspondence between modal fracture azimuth and crater shape at least suggests a causal relationship.

We have repeated this exercise for Barringer Crater as well as the Tswaing Crater near Pretoria in South Africa (formerly "Pretoria Saltpan Crater"). In the Kaibab carbonates that make up most of the target volume at Barringer, Roddy (1978) found a set of joints centered at approximately 30° clockwise from North and another centered at 304°. We find that maxima in the fourth harmonic of the rim-crest outline of Barringer Crater occur at 28° (and therefore also at 298° ⟺ 28−90°), in close agreement with the joint orientations and confirming the observations of Shoemaker (1960). (Kumar and Kring (2008) obtained a different result for the joint orientations at Barringer, although one of the authors took part in a more recent study (Poelchau et al., 2009) in which the former results of Shoemaker (1960) and Roddy (1978) were upheld.)

The Tswaing Crater is of similar size, age, and preservation, and the geology was characterized in detail by Brandt and Reimold (1995). In that study, the rim-crest outline was plotted along with

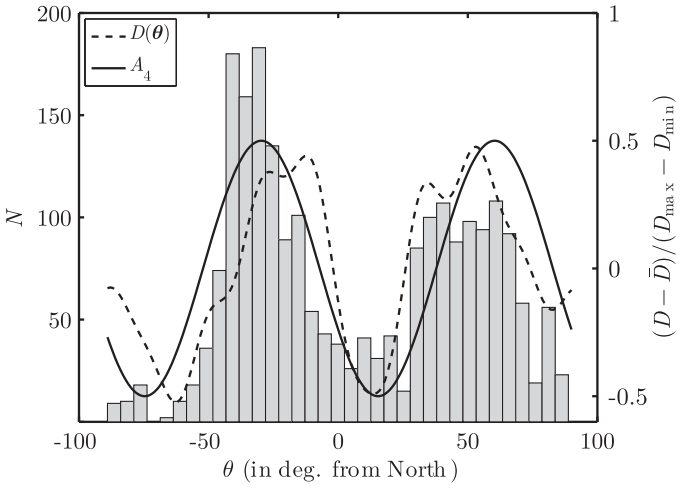

Fig. 16. Length-weighted histogram of the azimuths of linear troughs that occur in the sand-covered plains, and which reflect the orientation of underlying fractures (see Fig. 15). This distribution includes all troughs located within three crater radii of the Endurance Crater rim. Also plotted are two curves describing the crater planform, derived from the rim-crest outline: (i) the azimuthal diameter ($D(\theta)$, the diameter as a function of azimuth) expressed as a fraction of maximum deviation of diameter, as well (ii) as the phase of the fourth Fourier harmonic of the rim-crest outline (A_4). Modes in the distribution are almost exactly aligned or else aligned to within 10° of the square component of the crater planform, suggesting a causal relationship such as famously proposed for Barringer Crater by Shoemaker (1960).

rose histograms of the azimuths of joints and regional lineaments, although no quantitative analysis was undertaken to compare these. In Fig. 5 of that study, the modal bin of regional lineament azimuths is bounded by the range 21–37° clockwise from North, and the modal bin of joint azimuths measured from the immediate crater environs is bounded by the range 16–34°. We find that the peak of the fourth harmonic amplitude of the published rim-crest outline in this quadrant occurs at 21.5°, aligned with modal fracture azimuths in this case as well. This brings to three the number of well-preserved simple craters studied to date that exhibit this relationship.

5. Models of crater formation

5.1. Conceptual models

In this section we consider models of small impact crater formation that can be used to explain the observations presented so far. We begin with conceptual models that explore the consequences of different transient crater planforms and styles of slumping. Three of these are illustrated in Fig. 17. In each case the top frame shows the shape of the excavated or transient crater, which determines the shape of the hinge line (i.e., the flap hinge is everywhere located at a constant distance from the transient crater wall). The middle frame is the shape of the crater after slumping, and the bottom frame shows the resulting layering pattern.

In the case labeled A, a radially symmetric crater is excavated and the walls slump along pre-existing planes of weakness to form a polygonal crater, as proposed by Fulmer and Roberts (1963). That is, in this case the polygonal shape is the outcome of modification rather than asymmetries in crater growth. The result is a pattern of diamonds or lozenges that occur in the corners of the polygonal cavity. The flap hinge is preserved inside the crater walls only between corners, and has been destroyed in the corners. This pattern is not observed at Endurance or at any of the impact craters that we have examined at Meridiani Planum. According to model B, the transient crater has a polygonal (or non-circular) shape and maintains this shape after slumping. The polygonal shape is caused by asymmetries in crater growth and early modification does little to alter the planform. In this case, layering appears uniformly flat on the crater walls (as observed in some parts of Endurance such as the northwest wall). The distance of the hinge from the final crater walls is constant for all azimuthal positions. The hinge has everywhere been destroyed or else it is everywhere preserved.

In Model C, the transient crater exhibits a "stellate" or concave–cuspate planform, and the unstable prominences between vertices (henceforth called "knurls") slump during the early-stage modification. The outcome is a pattern of open smiles between corners of the polygon. For a slightly different shape of the hinge line or the radial section model (RSM), this can produce an almond or lens-shaped pattern instead, as shown in Section 3. We will refer to this pattern of layering as "lenticular-crescentic." In this case, the hinge is destroyed in between corners of the polygon, and plunges into the crater walls at the corners, where it is preserved. Since knurls are always formed in Model C, they might in some cases be preserved. This will be elaborated in Section 7; for now, we note that the only structure of this kind at Endurance, labeled γ and shown in part B of Figs. 2 and 4, is an expected outcome of

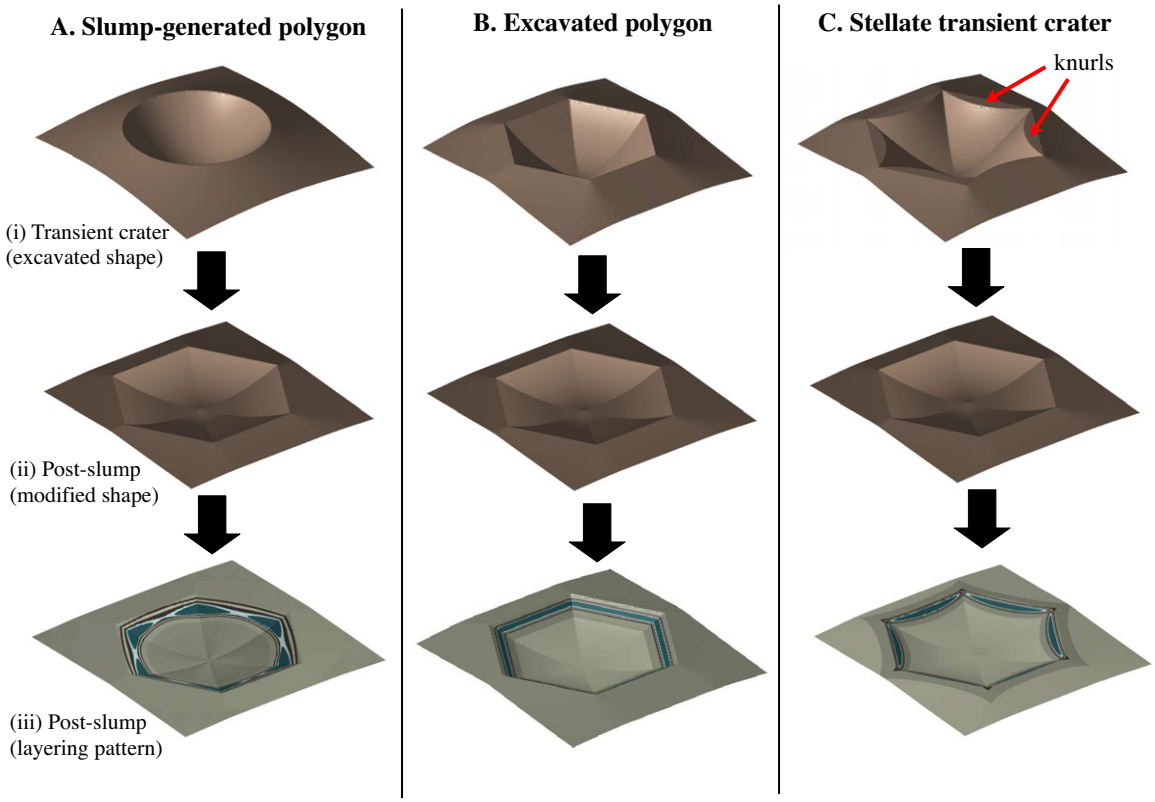

Fig. 17. Conceptual models of the formation of simple polygonal impact craters, and the implied pattern of layering in crater walls for horizontally-layered targets. The 3DLM with RSM1 was used to compute the layer pattern, assuming the hinge planform has the same shape as the transient crater. (A) A radially-symmetric transient crater is excavated, and then wall-slumping (as along pre-existing joints) creates a polygonal planform, producing a diamonds-in-corners pattern. (B) The transient crater is polygonal and maintains this shape after slumping. In this case, layers appear uniformly flat and have constant apparent thickness. (C) In stellate growth, the transient crater has a concave-cuspate planform, and the unstable prominences between vertices collapse ("knurls," marked with red arrows). The outcome is a lenticular-crescentic pattern of layering, with smiles or lenses between corners of the polygon. (For interpretation of the references to color in this figure legend, the reader is referred to the web version of this article.)

Fig. 18. Model illustration of "incurvate ejecta." Stellate crater growth (see Fig. 17, part C) in horizontally-layered targets is expected to produce a pattern of incurved layering in the continuous ejecta. Here, the flanks of the crater model in the last frame of part C of Fig. 17 have been eroded to reveal the pattern. Because layers in the overturned flap tend to be mixed even at modest distances from the rim, clear examples of this pattern are probably rare (cf. part B of Fig. 19).

"stellate" crater growth. On this view, the isolated lenses and open smiles labeled δ and ϵ as well as the entire west wall are "collapsed knurls."

A third consequence of Model C concerns the pattern of layering in the ejecta on the crater flanks. If crater growth is stellate, then strata in the overturned flap may reflect the concave–cuspate shape of the transient crater planform. That is, eroding the flanks of Model C reveals the incurved pattern of layering shown in Fig. 18. It is extremely rare, however, for layering in the continuous ejecta to remain coherent at large distances from the rim, so that "incurvate ejecta" are likely to be uncommon. An example is shown in part B of Fig. 19. The outline of continuous ejecta are unlikely to exhibit this pattern unless the asymmetric stellate growth begins at early times. Incurvate ejecta are not observed at Endurance where the crater flanks are mostly covered with sand, but all other features of Model C are evident. The pattern of layering in Fig. 2 suggests that Endurance was formed by a combination of growth styles illustrated by Models B and C. Many of the features that we have described as consequences of stellate growth (e.g., knurls, "open smiles" between corners, and incurvate ejecta) have been observed in other impact craters at Meridiani Planum captured by orbiter cameras, and some of these are shown in Fig. 19.

Layering in the walls at Barringer Crater exhibits a lenticular-crescentic pattern similar to that observed at Endurance. Like Endurance, Barringer Crater formed in a target made up of horizontal layers cut by widened conjugate fractures. Between corners of Barringer's west wall, the Moenkopi–Kaibab contact marks-out a smile shape (Poelchau et al., 2009), and a prominent sandstone bed also traces a smile between the corners of the west wall as well as the corners of the south wall (Shoemaker, 1960). Poelchau et al. (2009) suggest that this pattern is the result of increased uplift in the crater corners, noting the presence of inter-thrust wedges in some corners. Here we propose an alternative view, that the smile pattern is a natural consequence of crater growth being carried farther at the crater corners. That is, the lenticular-crescentic pattern is a straightforward result of the hinge deflecting horizontally outward rather than vertically upward at the corners.

The key to understanding which view is correct relates to where the hinge is preserved in the crater walls. At Barringer Crater, the pre-impact surface occurs in the thin Moenkopi siltstone (8 m in thickness) which pinches-out in three of the four crater corners (northeast, southwest, and southeast) as seen in the map of Shoemaker (1960). (This is analogous to the sand layer pinching-out in the C249 and C355 corners of Endurance Crater.) Moreover, two of these corners exhibit the telltale transition in structural dip that implies preservation of the flap hinge. In the southwest and southeast corners of Barringer Crater, beds of Kaibab dip steeply into the crater wall at low elevations, and become vertically oriented to steeply overturned (dipping craterward) higher on the wall. (The same pattern was noted at the ingress location near the southwest corner of Endurance in Section 2.) That is, the hinge is preserved in the southeast and southwest corners of Barringer Crater, and has been mostly destroyed between the corners (where the pre-impact surface contact is exposed). This is identical to the pattern expected for stellate crater growth. The inter-thrust wedges observed near the corners by Poelchau et al. (2009) may have also occurred in knurls that formed between corners of the concave-planform transient crater, and which collapsed at the onset of slumping.

5.2. Block-array model

It remains to be explained why some transient craters have a concave planform, or why the excavation flow can exhibit marked asymmetries so that crater growth is carried farther in some directions. We suggest the answer once again lies with the influence of fractures on the excavation flow. To examine this idea we consider the situation following the contact-and-compression stage, after the target has unloaded. Before impact, the target is cut in two orthogonal directions by a conjugate set of vertical joints akin to an array of columns, or to a 3-D array of cubes if horizontal layers are also planes of weakness. In the case of wide fractures like those found at Meridiani Planum, the cubes have a finite separation (i.e., the fractures have a measurable width). During the contact-and-compression stage, a fraction of the projectile's kinetic energy is converted into kinetic energy of the target, which in turn excavates the cavity (Melosh, 1989). Although the shock wave and excavation flow can form radial, conical, and concentric fractures (e.g., Kumar, 2005; Kumar and Kring, 2008), this will also reactivate

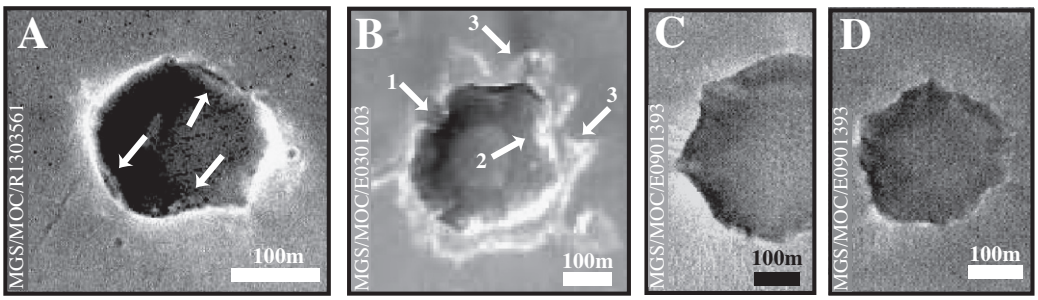

Fig. 19. Mars Orbiter Camera (MOC) images of impact craters at Meridiani Planum that exhibit features consistent with stellate crater growth: (A) Impact crater comparable in size to Endurance located several kilometers to the east with a lenticular-crescentic layer pattern, marked by lenses or smiles between corners of the polygonal planform; (B) impact crater exhibiting incurvate ejecta: (1) knurl, (2) possible smile-shaped layer, (3) lobes of incurvate ejecta. That the incurved pattern is not expressed on all sides suggests that polygonal growth (model B in Fig. 17) occurred to the west and south. (C) and (D) Craters with a concave planform, marked by possible knurls that have resisted slumping, located roughly 150 km east of Endurance Crater at Meridiani Planum.

fractures already present and which accommodate some of the deformation (Barosh, 1968).

At some distance from the site of impact, rock strength becomes comparable to deformational stresses of the shock wave. The target after unloading resembles its pre-impact state, although now subject to a spherically-symmetric impulse whose magnitude decays from the site of impact. Moreover, although the shock wave is highly inelastic, collisions between target-derived materials following release are approximately elastic. These insights allow us to simulate the excavation using a model of rigid solids responding to an impulse. Absent from this simplification are radial and concentric fractures introduced by the shock wave, and the obvious difference that fractures at Meridiani do not always connect.

The model initial condition and results are shown in Fig. 20. The first frame (at $t = 0$ s) shows a 3-D layer of cubes resting on a rigid plane ($25 \times 25 \times 5$ cubes). The positions of cubes have been randomly offset so that some are in contact with their neighbors while most are not, and the effective "fracture width" varies from 0% to 10% of the block size. Then, a spherically-symmetric impulse is applied whose magnitude decays inversely with the square of the radial distance from the bottom and center of the layer. A stronger decay with distance such as implied by Maxwell Z-models (Maxwell, 1977) does not affect the principal outcome: i.e., that a spherically-symmetric impulse causes asymmetric cavity growth. To simulate the evolution and identify major qualitative features of cavity growth, we have used the Open Dynamics Engine, a rigid-body dynamics simulator with friction and elastic collisions (Smith, 2006). From early times, the cavity is concave in planform (frame D of Fig. 20) and resembles the stellate model of crater growth (Model C in Fig. 17). Symmetry-breaking results from the anisotropy in effective shear strength. Initially, along the direction of fracture alignments, the impulse is only resisted by the inertia of distal blocks and by surface friction along fractures where cubes are in contact. The effective shear strength along this direction is therefore almost zero and has a maximum value in a direction 45° with respect to the fracture alignments. The anisotropy in target shear strength is a consequence of the effect described by Poelchau et al. (2009), who observed that the shear stress on each cube in a 3-D array is smallest in the direction of fracture alignments, and proposed this to explain the square shape of Barringer Crater.

In the simulation, columns and rows of blocks are preferentially expelled along the four directions defined by the conjugate set (see red arrows in part B of Fig. 20). These "slices" of the target are ejected from multiple free surfaces: the upper surface as well as the vertical surfaces that bound the array. (In reality, there is only one free surface, and the target accommodates the horizontal flow with compression and uplift.) As these slices are removed, the slightest asymmetry between layers on either side of the vacated slice implies a scissors-like displacement or tear fault. If real tear faults form in this way, then they cannot represent a sharp discontinuity, but rather imply a gap from which material has been removed. Blocks comprising the ejected slice are expelled at the highest velocities (from a given starting radius) and therefore travel farthest. Pre-cut "slices" of the target ejected in this manner may be the source of rays sometimes seen to radiate from corners of polygonal craters, as observed by Fulmer and Roberts (1963). That is, the model suggests a genetic relationship among crater rays, tear faults, and the polygonal planform. Gaps produced in this way might also become filled with injected debris. This may have occurred in some corners of Endurance Crater (e.g., C212, C249,

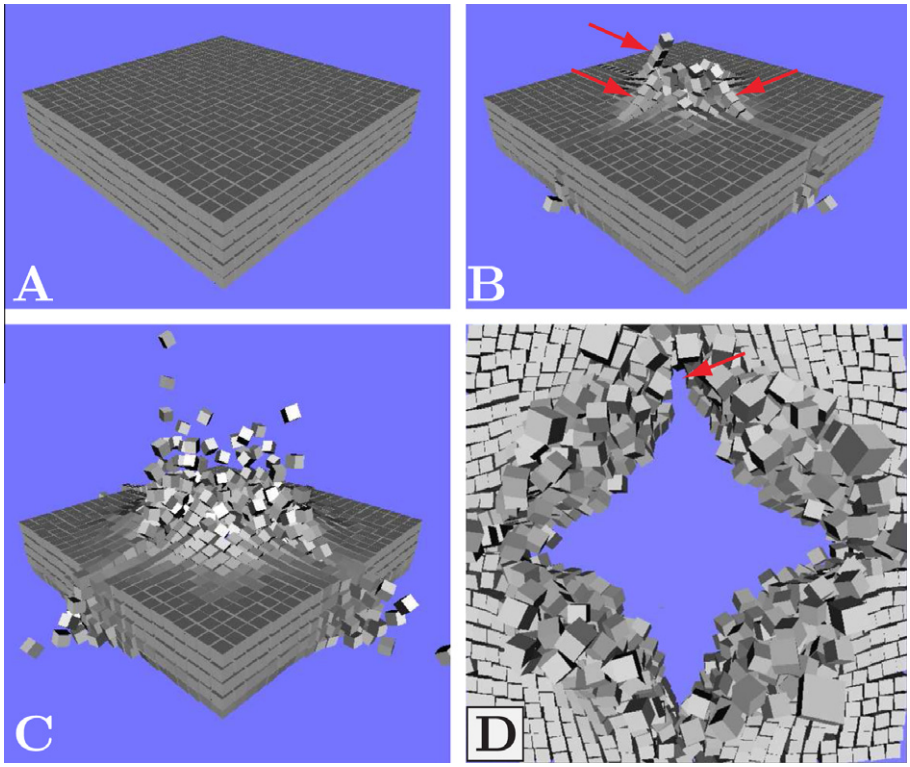

Fig. 20. A simulation illustrating the response of a 3-D layer of cubes ($25 \times 25 \times 5$) to a spherically-symmetric impulse that decays inversely with the square of distance from a point at the bottom-center of the layer. The layer is initially at rest on a rigid plane in frame (A). A marked asymmetry in the flow arises from a shear strength anisotropy: shear strength is smallest in the direction of fracture alignments. The resulting cavity has a concave planform (frame D), and is marked by gaps or notches at vertices (e.g., red arrow in frame D) where a slice has been cast out (red arrows in frame B). This process may indicate the origin of tear faults as well as crater rays (made up of material from an ejected slice or excavated notch) that sometimes emanate from corners of polygonal craters. The simulation was carried out using a rigid-body dynamics engine with elastic collisions and surface friction. The times corresponding to each frame are: (A) $t = 0$ s; (B) $t = 0.6$ s; (C) $t = 1.5$ s; (D) $t = 3.9$ s. (For interpretation of the references to color in this figure legend, the reader is referred to the web version of this article.)

C314, and C355), possibly forming structures like "β" in the north wall where a narrow slot appears filled with allochthonous debris (see parts A and G of Fig. 2). Large, fracture-bounded blocks may become wedged in the largest gaps; this may be the origin of rotated blocks such as α near C212 (Fig. 2, parts D and E).

The simulation in Fig. 20 illustrates the opening of a transient cavity that is concave in planform. Since the asymmetry in growth emerges as a consequence of shear strength anisotropy, it may be guessed that the asymmetry is greatest where this anisotropy is largest. In this respect, the uncommonly wide orthogonal fractures at Meridiani Planum represent an end-member scenario. In targets subdivided instead by hairline orthogonal joints, surface friction can be expected to play a more significant role, possibly reducing the concavity. For now, we speculate that an effective shear strength anisotropy – such as the comparison of bulk material strength and frictional stress along fractures – may largely determine the transient planform shape. The magnitude of the anisotropy may also partly determine the transition between strength and gravity-controlled excavation. Future work may find that the growth asymmetry emerges only very late in the excavation stage for large impacts, once the flow has sufficiently slowed. Understanding these effects in detail, as well as the effects of varying the mean fracture width, spacing and alignment, will require high-precision calculations with realistic strength models that address damage and failure.

The target volume in our simulations is a three-dimensional array of cubes, describing the case where layer boundaries also behave as planes of weakness. We also conducted simulations in which the volume is made up of vertical columns with a square cross-section in plan view. The result is qualitatively identical, in that a concave planform opens in this case as well. Also, the concave-cuspate planform is a robust result with respect to decreasing time-step size.

6. Structural class and prevalence

Many factors influence the shape and structure of simple impact craters, such as target strength properties, impact incidence angle and projectile velocity. Experiments, field studies, and numerical models have identified how some features of crater shape and structure are influenced or caused by variation of these parameters. Previous work has shown that the small number of terrestrial simple impact craters belong to at least two major categories (Shoemaker, 1960; Shoemaker and Eggleton, 1961; Shoemaker et al., 2005). Craters of the "Odessa type," based on Odessa Crater (Evans, 1961; Evans and Mear, 2000), tend to be small (diameter $\leqslant$200 m) and are shaped like a shallow inverted cone with small central bowl (walls slopes $\approx$30°). An anticlinal fold occurs in the walls, and the rim is mostly composed of ejecta rather than an overturned flap with inverted strata. Simple craters of the "Barringer type" are larger and bowl-shaped (upper wall slopes $\approx$45°), with a deeper breccia lens, and tend to exhibit an overturned flap with well-developed inverted stratigraphy.

Shoemaker (1960) suggested that the difference between these types arises from a different scaled penetration depth of the projectile. Odessa-type craters are thought to have a relatively shallow scaled depth of penetration (Shoemaker, 1960; Shoemaker and Eggleton, 1961) and form primarily by radial expansion, which may be more common for small craters where projectiles have been significantly slowed by the atmosphere (Shoemaker, 1963). In Barringer-type craters, with a larger scaled depth of penetration, excavation has the more prominent role. There are likely to be multiple factors that can influence the scaled depth of penetration, which on average may differ on Mars because of a thinner atmosphere, lower gravity, and different impactor source populations with a lower mean velocity.

Endurance Crater does not appear to fit neatly into the Odessa or Barringer categories. While its size, cavity shape, probable over-thrusts (west wall) and most-pristine wall slopes are consistent with the Odessa type, Endurance has a well-developed overturned flap with inverted strata. Sand covers the lower walls, precluding the search for an Odessa-type anticline. As mentioned, Endurance exhibits many of the other features of Barringer Crater, such as probable tear faults, a highly polygonal planform, a lenticular-crescentic pattern of layering, and preferential preservation of the hinge in corners. As shown in Section 4, these latter features appear related to the wide, orthogonal fractures in the target that bisect the square component of the crater planform. Barringer Crater also formed in a target with wide orthogonal fractures, in that case widened by dissolution (Roddy, 1978) rather than shrinkage. One of the lessons from Endurance Crater is that lenticular-crescentic layering and tear faults are

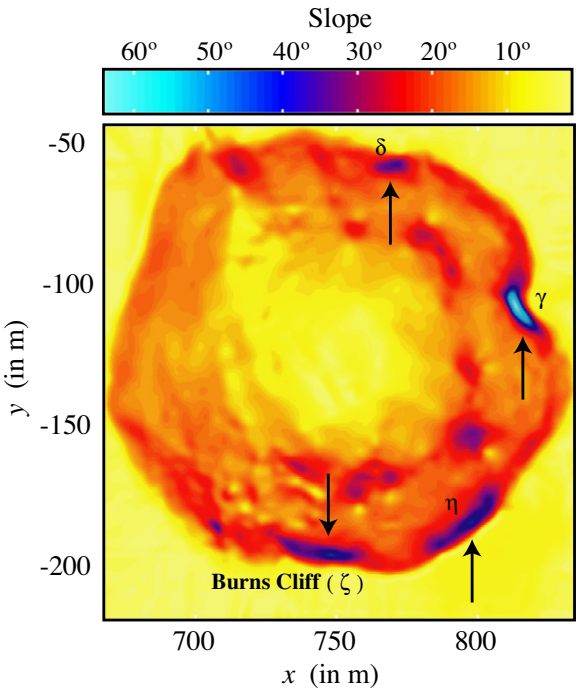

Fig. 21. Slope map derived from the Endurance Crater DEM, highlighting four locations along the upper wall where slopes exceed the repose angle of sand (~35°). All but one (i.e., Burns Cliff, labeled ζ) correspond to outcroppings of the dark bands in units II and III. In these three locations, a steep structural dip (>45°) is implied by the 3DLM. The slope map was Gaussian-filtered with σ = 5 m to mask fine seams in the DEM that otherwise appear prominently.

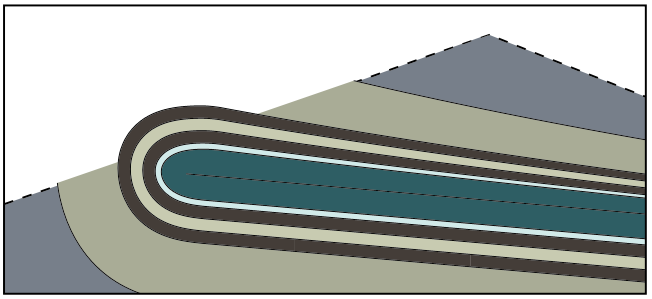

Fig. 22. A schematic of RSM2 illustrating why steep wall slopes correspond to outcroppings of the dark resistant bands in units II and III, as shown in Fig. 21: the dark layers are relatively resistant, so that overturned or vertical beds are eroded from the crater wall (e.g., the γ knurl in Fig. 12), in some cases becoming undermined and collapsing (e.g., the structure δ in parts A and G of Fig. 2).

strength-related features that may transcend the Barringer/Odessa distinction. Future research may illuminate whether the Barringer and Odessa categories are a useful distinction for simple craters on Mars, or at what size scale the transition typically occurs.

In addition to having wide orthogonal fractures, the Meridiani bedrock was among the most easily abraded using the Rock Abrasion Tool (RAT) of any class of rock encountered by Spirit or Opportunity, suggesting low material strength (Arvidson et al., 2004). Some aspects of crater structure at Meridiani Planum may be rare on Mars because the target materials exhibit these unusual properties.

7. Long-term modification of Endurance Crater

We suggested earlier that unit S corresponds to the plains sand layer, and that it is made up of sand alone. This layer may in some places compromise the crater rim because it is effectively strengthless. Wherever the sand is exposed, the wall slope is not likely to exceed the repose angle. Wall slopes are super-critical (>35°) in just four locations on the upper wall, as seen in the slope map of Fig. 21 (derived from the wide-baseline crater DEM). The symbol η marks a location (see Fig. 2, part C) where unit III is oriented vertically (i.e., according to the 3DLM and as observed in near-field imagery from PP2) and the sand unit is enclosed within the wall. The area labeled ζ in Fig. 21 is Burns Cliff, which is one of few locations where the usual stratigraphic sequence appears truncated. Units I–III are visible, but mixed rubble instead of sand overlies unit I, even though bedding planes in unit I dip at a shallow angle (~20°) into the crater wall. Here, it is possible the strengthless sand layer collapsed on a slope exceeding the repose angle, so that mixed flap debris came to lie directly on unit I.

Table 2
Structural strike (φ) and dip (ϑ) of bedding planes at the Karatepe location (plotted in Fig. 1). Reported are the median values derived from a bootstrap analysis (described in Appendix A), along with the span of the 95% confidence interval above ($\Delta\varphi_+$, $\Delta\vartheta_+$) and below ($\Delta\varphi_-$, $\Delta\vartheta_-$) the medians. The source of each measurement is identified by the rock ID number (n_{rock}, labeled in Fig. 1), a bedding plane ID number (λ, used only to show that measurements derive from different bedding planes on the same rock, and not labeled for reference elsewhere) and an image ID number ("img," see Table 6). Also reported are the point-cloud aspect ratio (γ), the angular separation between the normal of the fitted plane and the normal of the look-plane (ω), the look-plane proximity (κ), and the fraction of inter-point deviation (ξ). We have only reported results for which ($\Delta\vartheta_+ + \Delta\vartheta_-$) < 20° and ($\xi < 1$ or $\kappa > 1$).

n_{rock}	λ	img	φ	$\Delta\varphi_-$	$\Delta\varphi_+$	ϑ	$\Delta\vartheta_-$	$\Delta\vartheta_+$	γ	ω	κ	ξ
1	2	1	320.4	2.15	2.05	57.4	4.92	5.47	0.17	7.98	0.08	0.90
2	2	19	312.9	0.48	0.76	81.9	5.13	4.69	0.09	5.82	0.01	0.67
2	1	19	310.0	2.04	2.31	79.1	2.25	1.97	0.02	0.14	0.00	0.73
3	1	7	314.4	0.33	0.34	58.3	1.61	1.64	0.06	0.50	0.00	0.52
3	2	7	318.2	0.10	0.09	56.3	0.51	0.59	0.03	0.05	0.01	0.85
3	3	26	317.8	0.82	0.70	69.8	5.23	4.25	0.07	46.95	35.13	0.31
4	1	28	127.7	0.34	0.39	65.2	4.02	3.38	0.08	9.20	1.15	0.59
5	1	19	309.0	0.20	0.18	79.2	1.12	1.14	0.03	0.14	0.00	0.66
6	1	19	307.4	0.45	0.45	76.9	0.50	0.39	0.08	0.01	0.00	0.91
6	2	19	311.6	0.24	0.44	76.0	2.17	2.08	0.02	2.80	0.01	0.76
6	1	19	308.4	0.90	0.95	76.1	0.86	0.98	0.07	0.12	0.00	0.81
7	1	22	330.6	7.98	9.36	21.3	4.39	6.28	0.09	46.09	47.81	0.66
7	3	22	352.8	12.39	23.50	11.7	4.17	5.55	0.09	50.04	5.52	0.52
8	1	22	296.6	34.28	11.39	2.2	1.55	2.01	0.01	32.28	6.61	0.44
8	2	22	132.8	7.53	29.57	5.5	3.95	3.20	0.04	20.97	2.42	0.85
8	3	22	141.4	2.42	3.58	10.7	1.79	1.56	0.01	20.93	26.81	0.34
8	4	22	133.4	25.20	4.90	9.9	6.37	5.12	0.12	32.48	3.94	0.48
9	1	22	316.7	2.78	1.59	19.3	8.61	8.79	0.15	55.85	48.64	0.57
9	2	22	166.7	67.15	60.26	4.7	7.69	4.42	0.09	33.80	4.59	0.48
9	3	22	325.9	74.15	66.81	2.9	5.14	6.09	0.08	29.99	10.60	0.82
10	1	22	49.4	3.74	3.55	26.6	1.36	1.42	0.20	0.12	0.00	0.80
10	3	22	27.4	3.64	2.95	24.3	0.56	0.50	0.01	8.13	2.01	0.52
10	4	22	333.2	15.38	14.61	28.6	2.60	4.86	0.09	30.26	11.12	0.66
11	1	27	118.2	0.00	0.00	61.8	0.01	0.01	0.00	0.00	0.00	0.91
11	2	27	117.6	2.23	1.87	62.5	4.62	5.10	0.06	0.91	0.00	0.64
11	1	27	119.7	0.06	0.07	63.3	0.63	0.55	0.04	0.05	0.00	0.43
12	1	28	119.2	1.00	0.97	71.2	7.07	6.87	0.23	4.57	0.01	0.61
13	1	30	112.0	0.53	0.71	64.6	2.58	3.53	0.02	19.86	16.64	0.66
13	2	30	113.8	1.68	1.61	67.3	9.37	10.09	0.11	16.72	0.01	0.59
14	1	38	127.8	0.35	0.27	36.7	4.67	4.79	0.52	2.54	0.00	0.80
15	1	38	119.8	0.95	0.61	32.9	5.79	6.46	0.20	10.80	0.08	0.65
16	1	41	167.7	1.08	1.27	30.5	1.25	1.10	0.01	10.38	26.10	0.36
16	2	41	184.6	2.45	3.01	24.9	0.95	0.81	0.01	17.52	50.85	0.28
16	1	47	180.5	3.60	3.48	21.8	1.36	1.61	0.04	4.10	2.35	0.78
17	2	42	108.3	0.67	1.64	13.9	1.90	1.91	0.02	0.84	0.00	0.97
17	4	42	100.9	4.06	2.82	12.2	3.24	3.52	0.04	0.94	0.00	0.83
17	5	42	112.7	3.99	2.98	7.0	2.93	1.79	0.01	8.78	0.03	0.59
68	1	95	105.0	9.63	7.15	9.8	0.98	1.31	0.04	0.60	0.01	0.84
68	2	102	137.1	3.76	3.80	62.4	6.96	7.84	0.30	4.56	0.00	0.92
69	1	96	113.7	0.59	0.63	57.4	4.10	4.87	0.10	40.68	9.55	0.22
69	2	102	110.3	2.88	2.55	35.7	6.07	5.22	0.14	6.07	0.00	0.69
69	1	96	108.7	2.09	2.18	40.7	3.83	4.79	0.10	16.21	7.76	0.70
70	1	96	98.4	4.07	3.29	16.6	1.15	1.33	0.06	0.37	0.02	0.84
71	1	105	104.7	1.54	1.28	32.5	2.28	2.15	0.10	2.36	0.05	0.46
71	2	105	112.6	1.30	0.96	21.6	2.36	2.61	0.10	1.84	0.00	0.68
72	1	100	144.8	0.49	0.45	38.2	4.25	4.12	0.13	9.01	0.06	0.69
73	1	104	184.3	9.49	10.41	32.1	0.56	1.57	0.08	4.36	0.01	0.66
74	1	20	320.7	0.71	0.60	63.2	0.33	0.19	0.00	0.11	0.01	0.63

Three of four locations on the upper walls having super-critical slopes (Fig. 21) correspond to outcroppings of the dark resistant bands at the top of units II and III which, according to the 3DLM, are steeply dipping in each location. As described in Section 5, the only knurl preserved at Endurance Crater is labeled γ on the east wall in Figs. 2, 4, 12, and 21, which we interpret as buttressed and protected by steeply-dipping beds of the more resistant dark band at the top of unit III on its craterward face. Knurls at Endurance (and other craters at Meridiani) may have eroded-out from crater walls (as illustrated in Fig. 22) and persisted because of the protection offered by the dark bands in units II and III until undercut by erosion. The fourth location with super-critical slopes corresponds to an outcropping of the dark bands in units II and III at the margin of a collapsed knurl labeled δ (Fig. 2, parts A and G). The debris from this collapsed structure can be seen at a lower elevation on the crater wall. Piles of debris at half the crater depth occur in several locations and may correspond to the remains of other collapsed knurls (Fig. 4, part B).

Saltation of the plains sand abrades the comparatively soft Meridiani outcrops, in some locations forming ventifact wind-shadows behind hard hematitic concretions, which indicate the prevailing wind direction. Most of these features point 15° north of due west (Sullivan et al., 2005). Accordingly, Grant et al. (2006) observed that the west wall of Endurance is the most eroded, having the most shallow slope and lowest rim. Our work confirms these results: the flap hinge has been completely removed from the west and north walls, and is mostly preserved along the east and southeast walls of the crater (such as at position η in Fig. 2; see also Figs. 7 and 9). The only surviving knurl (γ) is also located in the east wall. Fig. 7 shows that the hinge (and hence the transient crater planform) closely mimics the present-day planform. Wind-blown sand abrasion has therefore not dramatically altered the overall shape of the crater outline, apart from possibly undermining knurls as described above. Instead, the crater planform has been expanded in the direction of the prevailing winds, primarily to the west and northwest.

Table 3
Structural strike (φ) and dip (ϑ) of bedding planes at the egress Waypoint location (plotted in Fig. 1). Reported are the median values derived from a bootstrap analysis (described in Appendix A), along with the span of the 95% confidence interval above ($\Delta\varphi_+$, $\Delta\vartheta_+$) and below ($\Delta\varphi_-$, $\Delta\vartheta_-$) the medians. The source of each measurement is identified by the rock ID number (n_{rock}, labeled in Fig. 1), a bedding plane ID number (λ, used only to show that measurements derive from different bedding planes on the same rock, and not labeled for reference elsewhere) and an image ID number ("img," see Table 6). Also reported are the point-cloud aspect ratio (γ), the angular separation between the normal of the fitted plane and the normal of the look-plane (ω), the look-plane proximity (κ), and the fraction of inter-point deviation (ξ). We have only reported results for which ($\Delta\vartheta_+ + \Delta\vartheta_-$) < 20° and ($\xi < 1$ or $\kappa > 1$).

n_{rock}	λ	img	φ	$\Delta\varphi_-$	$\Delta\varphi_+$	ϑ	$\Delta\vartheta_-$	$\Delta\vartheta_+$	γ	ω	κ	ξ
18	1	50	176.6	7.09	18.52	3.9	1.56	1.58	0.01	17.28	1.46	0.37
18	2	50	92.8	2.45	1.51	15.5	3.02	2.49	0.04	19.15	19.47	1.00
19	2	90	277.3	3.06	3.21	18.4	1.95	2.20	0.03	6.42	1.90	0.87
19	3	90	243.3	5.06	4.75	16.7	0.69	0.74	0.02	2.13	0.03	0.73
47	1	90	296.1	0.82	1.42	12.0	0.93	0.87	0.01	0.37	0.00	0.95
48	1	85	32.5	1.41	2.38	13.2	1.16	1.01	0.01	0.39	0.01	0.68
49	1	85	213.8	13.76	17.96	26.5	6.25	9.82	0.24	21.15	0.53	0.76
50	1	86	184.6	14.54	38.25	5.7	1.51	2.10	0.04	9.53	2.15	0.94
50	2	86	118.3	16.09	6.07	11.0	4.89	3.86	0.08	14.30	0.32	0.96
50	3	89	293.6	2.08	2.66	16.6	3.86	4.92	0.07	29.48	98.50	0.48
50	4	89	21.2	19.37	16.66	11.5	0.64	1.08	0.12	3.74	0.06	0.98
50	5	89	84.9	46.65	13.83	9.5	4.71	7.38	0.49	3.13	0.01	0.83
50	6	89	340.6	31.96	66.44	5.6	1.77	6.65	0.20	18.97	4.69	0.74
50	7	89	298.0	6.26	3.29	10.3	4.12	5.40	0.05	38.31	58.22	0.43
51	1	86	301.0	1.93	3.56	15.6	7.26	7.38	0.09	80.90	106.25	0.40
51	2	86	300.5	16.84	14.55	3.6	6.40	6.59	0.11	64.98	6.46	0.32
51	3	87	106.8	38.34	32.23	3.6	4.60	3.55	0.03	67.01	19.79	0.36
51	2	87	121.2	22.40	24.89	2.2	10.20	9.11	0.14	56.79	1.11	0.29
52	1	86	123.9	51.37	53.63	2.5	4.45	3.91	0.05	35.10	0.73	0.34
52	2	87	123.9	34.04	12.30	13.0	9.85	8.11	0.21	18.43	0.07	0.95
53	1	86	295.4	0.65	0.66	23.8	5.69	5.25	0.07	75.68	53.02	0.33
53	3	86	297.4	1.35	3.45	20.3	10.02	9.19	0.15	82.56	0.98	0.45
53	1	87	294.2	0.89	0.88	17.3	4.34	4.20	0.06	79.95	66.65	0.27
54	1	86	259.6	4.07	5.47	22.8	1.26	1.49	0.01	5.77	1.17	0.86
54	4	89	137.0	0.82	0.52	19.1	0.79	1.03	0.22	0.07	0.01	0.91
55	2	86	259.7	4.62	5.22	15.6	0.74	0.87	0.01	13.94	16.60	0.65
55	3	89	250.7	20.04	14.96	9.0	2.06	2.98	0.05	23.20	26.74	0.35
55	4	89	279.5	4.28	3.53	14.9	2.33	2.30	0.02	20.30	75.57	0.42
55	5	89	173.0	44.70	48.24	4.1	1.75	1.83	0.06	7.10	0.29	0.74
55	6	89	279.6	4.21	3.41	9.6	1.95	2.55	0.02	20.14	58.07	0.35
56	1	86	249.7	70.04	87.63	1.0	2.08	1.25	0.01	13.93	2.54	0.34
57	1	86	106.9	40.78	10.03	6.3	4.41	3.88	0.07	14.81	0.66	0.75
57	3	89	318.5	2.12	2.40	13.5	1.72	1.98	0.01	16.10	162.96	0.39
58	1	87	135.1	1.48	2.18	25.2	6.60	6.20	0.10	48.75	7.71	0.77
59	1	89	243.6	3.39	4.71	10.0	0.58	0.55	0.01	0.21	0.00	0.86
59	2	90	191.9	8.11	10.21	14.4	1.03	1.61	0.09	0.20	0.02	0.87
60	1	90	341.5	3.08	2.83	27.9	0.35	0.38	0.01	4.73	7.69	1.00
60	2	91	347.1	2.01	2.04	25.0	0.12	0.10	0.01	0.51	0.00	0.90
61	1	91	285.9	7.76	9.11	38.2	5.25	7.50	0.17	37.53	16.16	0.41
62	1	90	188.7	7.68	6.48	17.3	0.76	0.74	0.03	10.23	17.56	0.65
63	3	91	309.3	1.25	1.45	8.1	0.09	0.11	0.06	0.01	0.02	0.64
64	1	92	10.0	7.69	7.02	10.1	1.66	2.47	0.02	11.43	19.15	0.81
64	2	93	65.3	45.27	53.53	3.0	0.82	2.16	0.04	4.49	0.03	0.90
65	1	92	214.0	4.71	4.98	43.7	3.91	3.93	0.17	4.24	0.01	0.64
66	1	92	273.4	7.10	10.65	31.7	1.98	1.98	0.11	32.52	7.23	0.66
67	1	93	42.0	26.35	16.27	11.0	1.22	2.28	0.05	17.40	1.40	0.67

8. Conclusions

The observations acquired during Opportunity's campaign within and around Endurance Crater offer an uncommon chance to study a small, well-preserved impact crater that formed in a layered target cut by wide, conjugate fractures. The lenticular-crescentic pattern of layering in the upper crater walls and selective preservation of the hinge in corners implies that crater growth was carried significantly farther in some directions. According to this "stellate growth" model, the transient crater had a concave-cuspate planform. Most of the craterward prominences that formed between vertices of the transient crater planform ("knurls") probably collapsed at the onset of slumping, although Endurance Crater retains one example to the present day. Many of the features observed at Endurance and predicted by the stellate growth model (e.g., knurls, incurvate ejecta, and lenticular-crescentic layering) were identified in other craters at Meridiani Planum in MOC images.

Two prominent and orthogonal modes in the distribution of target fracture azimuths are aligned with the square component of the Endurance Crater planform. This relationship was long ago shown for Barringer Crater, and we find that it also holds for Tswaing Crater in South Africa. Barringer also exhibits lenticular-crescentic layering with selective preservation of the hinge in corners, implying stellate crater growth. Endurance Crater has features both of Odessa-type and Barringer-type craters, falling neatly into neither category.

We have modeled crater growth in aligned-fracture targets by simulating the effects of a spherically-symmetric impulse acting on a 3-D layer of cubes or columns using a rigid-body dynamics simulator. This simple model reveals that columns and rows of blocks are ejected preferentially along the direction of alignments, producing a transient cavity that is concave-cuspate in planform. Notches form where slices of the target are removed, and likely correspond to tear faults like those observed at Endurance and Barringer Craters. The material ejected from these notches may form the rays sometimes observed to emanate from corners of polygonal craters.

Our structural model of Endurance was used to estimate the path in 3-D of the overturned flap hinge, which roughly mimics

Table 4
Part I of structural strike (φ) and dip (ϑ) of bedding planes at the Burns Cliff location (plotted in Fig. 1). Reported are the median values derived from a bootstrap analysis (described in Appendix A), along with the span of the 95% confidence interval above ($\Delta\varphi_+$, $\Delta\vartheta_+$) and below ($\Delta\varphi_-$, $\Delta\vartheta_-$) the medians. The source of each measurement is identified by the rock ID number (n_{rock}, labeled in Fig. 1), a bedding plane ID number (λ, used only to show that measurements derive from different bedding planes on the same rock, and not labeled for reference elsewhere) and an image ID number ("img," see Table 6). Also reported are the point-cloud aspect ratio (γ), the angular separation between the normal of the fitted plane and the normal of the look-plane (ω), the look-plane proximity (κ), and the fraction of inter-point deviation (ξ). We have only reported results for which ($\Delta\vartheta_+ + \Delta\vartheta_-$) < 20° and ($\xi$ < 1 or κ > 1).

n_{rock}	λ	img	φ	$\Delta\varphi_-$	$\Delta\varphi_+$	ϑ	$\Delta\vartheta_-$	$\Delta\vartheta_+$	γ	ω	κ	ξ
20	1	53	130.8	4.62	7.79	14.7	2.66	2.21	0.06	18.75	11.48	0.77
20	1	62	109.6	1.49	2.53	36.0	5.49	3.99	0.10	29.42	16.37	0.88
21	1	66	174.7	1.72	1.93	10.3	0.13	0.13	0.03	0.05	0.01	0.91
21	2	66	172.5	6.84	7.78	10.1	0.41	0.56	0.04	1.76	0.09	0.76
21	2	54	132.5	1.73	2.13	21.0	1.38	1.32	0.02	0.74	0.00	0.85
21	1	54	127.1	1.61	1.39	25.5	1.21	1.61	0.01	4.15	1.59	0.60
21	2	63	123.5	0.36	0.40	29.9	0.54	0.50	0.02	0.10	0.01	0.33
21	2	63	123.6	0.05	0.05	30.9	0.40	0.42	0.06	0.02	0.03	0.53
21	1	63	118.3	0.89	0.73	37.0	1.13	1.40	0.01	5.72	4.49	0.47
21	1	74	138.7	2.74	2.63	18.2	1.19	1.41	0.03	11.49	13.06	0.33
21	2	74	137.1	3.19	3.62	17.9	1.55	1.73	0.05	13.10	50.85	0.26
21	2	74	136.8	3.43	3.66	17.8	1.62	1.87	0.05	13.20	68.72	0.28
21	1	74	150.4	5.20	7.28	14.0	1.49	1.43	0.06	6.23	7.35	0.38
22	1	54	134.6	2.90	2.99	12.1	0.72	0.81	0.04	0.18	0.00	0.93
22	1	63	116.1	0.62	0.66	23.7	0.71	0.68	0.09	0.06	0.01	0.45
22	2	63	121.4	1.84	2.07	20.3	1.43	1.51	0.16	0.54	0.00	0.64
22	1	70	114.7	2.44	3.27	21.5	2.69	2.61	0.10	17.38	89.22	0.50
22	1	71	111.1	2.60	3.20	24.0	3.69	3.98	0.17	21.23	83.48	0.74
23	2	56	101.5	2.10	2.27	15.4	0.88	0.83	0.05	0.02	0.00	0.90
24	1	57	102.7	0.89	0.91	15.8	1.62	1.77	0.01	11.91	37.98	0.44
24	2	57	96.9	0.67	0.69	20.1	2.13	2.37	0.02	15.97	40.77	0.43
25	1	60	112.4	1.27	1.35	30.0	4.21	5.86	0.07	25.11	20.03	0.53
25	1	60	109.9	3.67	2.79	20.6	5.08	6.01	0.10	15.08	1.20	0.92
25	1	83	87.6	9.57	6.84	19.4	2.78	3.24	0.11	8.65	0.27	0.88
26	1	84	317.4	7.29	15.28	18.2	7.26	7.46	0.31	16.67	0.38	0.84
27	3	73	192.8	3.06	2.96	19.5	0.63	0.76	0.15	0.04	0.00	0.91
28	1	64	167.9	9.14	8.60	13.6	0.60	0.63	0.12	0.32	0.00	0.74
28	2	64	169.1	1.25	1.62	13.4	0.33	0.40	0.07	0.03	0.00	0.99
28	3	65	205.2	16.23	12.17	7.8	0.89	1.40	0.09	1.42	0.01	0.87
28	1	65	122.0	10.41	12.05	14.5	1.68	2.53	0.06	11.33	4.16	0.81
28	1	72	134.5	23.00	26.54	12.7	1.51	3.60	0.15	17.31	5.09	0.73
28	4	72	283.3	1.01	0.77	27.2	3.46	3.04	0.12	4.13	0.02	0.85
28	1	73	138.1	14.57	13.63	13.3	0.79	1.15	0.07	15.84	12.82	0.60
28	3	73	209.9	6.24	5.58	15.5	0.88	0.95	0.05	0.16	0.00	0.97
28	2	73	219.5	5.22	3.89	13.6	1.38	1.57	0.03	1.60	0.01	0.87
29	1	72	173.3	6.29	6.08	18.5	0.43	0.36	0.02	3.63	0.01	0.83
29	2	73	141.2	21.33	35.87	15.3	1.94	5.35	0.32	15.45	0.20	0.73
29	1	73	177.9	16.87	18.76	14.5	0.58	1.03	0.11	5.78	0.01	0.81
30	1	64	134.5	3.43	3.09	12.8	0.54	0.72	0.01	8.85	26.39	0.69
30	3	64	129.4	3.84	3.87	13.4	0.78	0.92	0.01	9.00	82.09	0.89
30	4	64	133.3	5.37	5.32	13.2	0.67	0.95	0.01	6.83	31.80	1.39
30	2	65	113.9	2.61	2.66	18.6	1.47	1.74	0.03	17.30	109.70	1.00
30	1	65	123.0	2.85	2.71	16.3	0.98	1.10	0.02	13.36	19.45	0.80

the 3-D trace of the modern crater rim. This implies that the present-day shape of Endurance Crater was mostly determined by excavation rather than long-term modification by wind-mediated erosion. Erosion has mostly destroyed the hinge in the south, west and north walls, widening the crater rather than significantly altering its planform.

Acknowledgments

We would like to acknowledge the thousands of engineers and scientists who designed and built the Mars Exploration Rovers, the Mars Reconnaissance Orbiter, and the Mars Global Surveyor spacecraft as well as their instrument payloads. We also heartily acknowledge the contributions of the entire Athena Science Team, and all those who, along with some of the authors, took part in the planning of Opportunity's observations during the Endurance Crater campaign. We are also grateful to Erwan Mazarico, Shoshanna Cole, Jeffrey Andrews-Hanna, and Ian Garrick-Bethell for insightful discussions. We would like to thank Drew Barringer and the Meteor Crater Company for their assistance and for generously granting access to Barringer Crater in January of 2008. We extend our thanks to Michael Poelchau for providing an immensely helpful review of the manuscript. In conducting this research and preparing the report we made use of free and open-source software and would like to warmly acknowledge the developer communities for Emacs, Inkscape, LATEX, and GNU/Linux.

Appendix A. Estimates of bedding plane orientation and error analysis

In this appendix we describe how the strike and dip of bedding planes are measured and supply an estimate of the error in these measurements. These results are reported for rocks on the south wall at Karatepe in Table 2, the egress "Waypoint" location in Ta-

Table 5
Part II of structural strike (φ) and dip (ϑ) of bedding planes at the Burns Cliff location. (See Table 4.)

n_{rock}	λ	img	φ	$\Delta\varphi_-$	$\Delta\varphi_+$	ϑ	$\Delta\vartheta_-$	$\Delta\vartheta_+$	γ	ω	κ	ξ
31	4	66	179.1	12.49	11.15	17.6	1.81	2.58	0.05	8.97	1.75	0.70
31	2	64	126.8	3.78	3.70	29.8	3.98	5.33	0.06	27.79	25.63	0.47
31	3	64	126.8	3.06	2.63	34.1	2.52	3.32	0.03	19.69	22.33	0.44
31	2	72	146.0	13.96	16.29	22.8	2.31	3.81	0.15	17.95	5.70	0.78
31	2	73	180.3	9.21	8.54	20.1	0.72	0.87	0.14	5.29	0.39	0.54
31	3	73	123.5	5.06	5.46	29.3	3.38	4.57	0.07	33.05	63.14	0.38
31	2	73	153.8	11.19	11.23	15.7	0.88	1.52	0.07	15.86	19.34	0.42
31	2	73	150.3	8.50	8.80	18.1	0.97	1.39	0.05	16.32	14.89	0.44
32	5	64	173.9	4.39	4.99	16.7	0.62	0.71	0.27	0.05	0.01	0.95
32	5	64	212.8	38.91	19.22	19.8	5.19	8.33	0.40	9.85	0.00	0.75
32	6	65	165.9	14.39	15.67	15.0	0.66	0.87	0.08	2.38	0.01	0.97
32	2	65	164.9	8.02	9.61	13.7	0.21	0.48	0.04	3.11	0.00	0.88
32	1	72	229.7	2.80	3.27	22.4	0.88	1.11	0.02	7.79	4.93	0.58
32	8	72	231.9	4.49	3.91	11.3	0.80	0.62	0.01	4.17	1.34	0.25
33	1	65	136.0	4.35	4.29	26.4	0.72	0.51	0.03	2.89	0.06	0.76
33	2	65	116.3	5.51	5.66	22.3	2.83	3.76	0.09	16.65	15.07	0.64
33	2	70	103.4	4.03	4.40	39.8	7.25	9.19	0.17	46.36	11.35	0.39
33	2	71	102.9	3.41	3.33	44.1	6.36	7.97	0.14	51.06	38.98	0.40
33	3	71	108.7	10.65	13.64	26.8	6.07	8.72	0.22	29.67	11.56	0.65
34	1	68	127.6	1.71	1.89	21.0	1.50	1.46	0.04	6.95	19.98	1.08
34	1	69	128.7	2.04	2.22	21.0	1.56	1.65	0.06	6.07	4.87	0.77
35	1	70	122.8	8.47	10.62	20.6	3.51	4.76	0.15	14.44	4.83	0.50
35	5	71	139.1	10.88	11.39	36.2	1.81	1.60	0.21	3.05	0.00	0.95
35	1	71	131.8	15.88	31.62	18.3	4.54	6.74	0.38	10.18	0.01	0.91
35	2	71	125.7	3.38	2.84	23.2	1.23	1.87	0.02	13.51	41.11	0.42
36	1	75	196.7	0.43	0.38	31.6	0.22	0.25	0.03	0.01	0.01	0.44
36	2	75	209.7	3.08	3.02	19.9	0.35	0.22	0.04	0.29	0.00	0.70
36	2	76	186.3	11.77	11.68	22.2	1.39	1.66	0.17	6.14	0.00	0.81
37	1	75	300.7	2.56	2.66	18.0	0.75	0.84	0.02	0.89	0.01	0.80
37	1	75	311.8	3.61	4.56	17.7	1.14	0.91	0.02	3.08	0.39	0.78
37	2	76	324.0	11.95	11.06	21.5	0.57	0.72	0.18	4.58	0.00	0.74
37	1	76	304.0	3.35	3.53	18.7	1.05	1.18	0.03	0.92	0.01	0.90
37	1	76	313.5	4.80	4.77	18.3	0.79	0.87	0.02	3.20	0.05	0.91
38	1	76	232.5	6.02	6.50	33.6	0.61	0.98	0.09	14.36	10.12	0.72
39	1	78	332.0	3.19	3.80	22.0	1.44	1.54	0.11	0.57	0.00	0.87
39	2	78	306.2	2.85	2.72	42.9	3.56	4.77	0.09	24.03	12.44	0.57
39	2	79	337.3	5.65	5.77	26.6	1.89	2.26	0.15	1.12	0.01	0.98
40	1	78	250.7	0.87	0.85	22.9	0.90	1.04	0.02	0.87	0.00	0.71
40	2	78	250.2	3.58	2.90	20.9	2.10	2.30	0.09	2.65	0.00	0.93
40	3	78	228.3	63.25	31.11	3.9	1.94	3.20	0.09	17.34	1.27	0.61
40	5	78	250.9	11.66	5.60	13.7	4.27	4.69	0.25	8.99	0.04	0.71
40	5	79	243.4	19.42	9.28	8.0	2.93	3.21	0.11	14.30	2.53	0.67
40	5	79	240.6	22.86	10.41	7.5	2.35	2.63	0.09	14.53	0.41	0.60
40	6	79	296.9	2.46	4.42	13.5	2.81	2.51	0.06	5.21	0.07	0.95
41	1	78	358.3	19.13	21.49	26.1	2.79	5.74	0.38	5.36	0.00	0.87
42	2	80	340.0	4.81	4.88	20.6	1.08	1.18	0.07	0.43	0.01	0.98
42	3	80	342.0	4.40	4.57	20.4	0.74	0.73	0.11	0.03	0.01	0.94
42	5	81	299.0	6.81	17.99	20.6	8.76	7.79	0.53	4.44	0.00	0.75
43	1	80	17.1	22.26	25.97	8.2	0.82	0.96	0.07	15.09	4.16	0.77
44	1	82	90.1	0.28	0.23	7.8	0.14	0.12	0.05	0.00	0.01	0.72
45	1	84	62.6	5.10	4.17	16.6	1.02	1.10	0.03	1.63	0.01	0.69
46	1	84	141.8	9.82	13.52	11.3	2.70	3.92	0.11	26.09	22.68	0.36

Table 6
Index of MER-B Pancam and Navcam image files listed in Tables 2–5. These are the left-eye images of a stereo pair used to estimate strike and dip of bedding planes. "FFL" files are linearized versions of the raw "EFF" data products: i.e., with camera-lens distortions removed.

img	Filename	img	Filename
1	1P140084884FFL3160P2372L7M1.IMG	66	1N153485606FFL37MIP0894L0M1.IMG
5	1P140259198FFL3174P2376L7M1.IMG	68	1P153749290FFL37MIP2271L2M1.IMG
7	1P140259765FFL3174P2376L7M1.IMG	69	1P153749423FFL37MIP2271L7M1.IMG
16	1P140527301FFL3182P2379L7M1.IMG	70	1P153749562FFL37MIP2271L2M1.IMG
17	1P140527652FFL3182P2379L7M2.IMG	71	1P153749936FFL37MIP2271L7M1.IMG
19	1P140528084FFL3182P2379L7M1.IMG	72	1P153750092FFL37MIP2271L2M1.IMG
20	1P140528581FFL3182P2379L7M1.IMG	73	1P153750471FFL37MIP2271L7M1.IMG
22	1P140530030FFL3182P2379L7M1.IMG	74	1P153750999FFL37MIP2271L7M2.IMG
26	1P141947885FFL3200P2382L7M1.IMG	75	1P153839111FFL37MIP2272L2M1.IMG
27	1P142565907FFL3221P2389L7M1.IMG	76	1P153839487FFL37MIP2272L7M1.IMG
28	1P142566000FFL3221P2389L7M1.IMG	77	1P153927216FFL37MIP2273L7M3.IMG
30	1P142566092FFL3221P2389L7M2.IMG	78	1P153927863FFL37MIP2273L2M1.IMG
31	1P142566419FFL3221P2389L7M1.IMG	79	1P153928248FFL37MIP2273L7M1.IMG
33	1P142567125FFL3221P2389L7M1.IMG	80	1P154016243FFL37MIP2274L2M2.IMG
38	1P142744956FFL3221P2391L7M1.IMG	81	1P154016650FFL37MIP2274L7M1.IMG
41	1N143374719FFL3300P1921L0M1.IMG	82	1P154104865FFL37MIP2275L7M1.IMG
42	1P143717728FFL3300P2530L7M1.IMG	83	1P154105597FFL37MIP2275L2M2.IMG
46	1P144163942FFL3336P2406L7M1.IMG	84	1P154105987FFL37MIP2275L7M2.IMG
47	1N144178155FFL3352P1915L0M1.IMG	85	1N154464945FFL3853P1992L0M1.IMG
48	1N152335995FFL37HNP1909L0M1.IMG	86	1N154464996FFL3853P1992L0M2.IMG
49	1N152336047FFL37HNP1909L0M1.IMG	87	1N154465047FFL3853P1992L0M1.IMG
50	1N152511359FFL37IFP0664L0M1.IMG	89	1N154552403FFL3897P1992L0M2.IMG
51	1N152777120FFL37KDP1981L0M1.IMG	90	1N154552440FFL3897P1992L0M1.IMG
52	1N152781934FFL37KDP1954L0M1.IMG	91	1N154552477FFL3897P1992L0M1.IMG
53	1P152861555FFL37KDP2440L7M1.IMG	92	1N154994864FFL38ARP1996L0M2.IMG
54	1P152861698FFL37KDP2440L7M1.IMG	93	1N154994901FFL38ARP1996L0M1.IMG
56	1P152951221FFL37LJP2442L7M1.IMG	94	1N154994952FFL38ARP1996L0M1.IMG
57	1P152951626FFL37LJP2442L7M1.IMG	95	1N155088037FFL38D7P1996L0M1.IMG
60	1N153045268FFL37LJP1909L0M1.IMG	96	1N155088089FFL38D7P1996L0M1.IMG
61	1N153045487FFL37LJP1909L0M1.IMG	97	1N155175243FFL38ENP1998L0M1.IMG
62	1P153127782FFL37LJP2444L2M1.IMG	100	1N155356453FFL38EVP1996L0M1.IMG
63	1P153128010FFL37LJP2444L7M1.IMG	102	1N155527259FFL38EVP1950L0M1.IMG
64	1P153128119FFL37LJP2444L2M1.IMG	103	1N155707773FFL38EVP1724L0M1.IMG
65	1P153128410FFL37LJP2444L7M2.IMG	104	1N155707896FFL38EVP1724L0M1.IMG

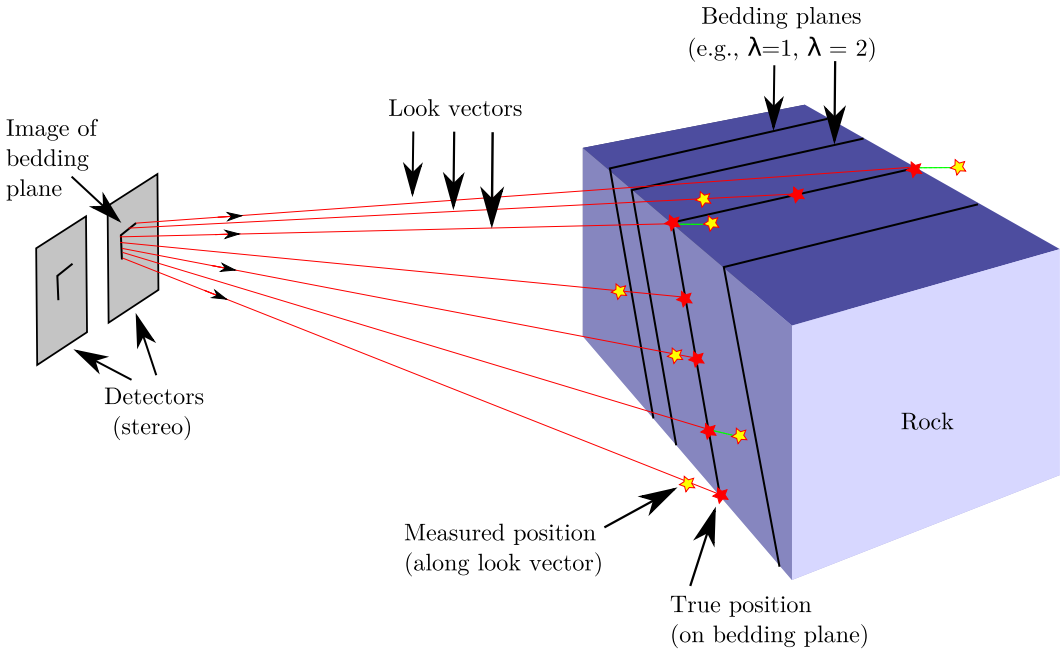

Fig. 23. Illustration of stereogrammetric measurement of bedding plane orientations with optics omitted. The rock at right has bedding planes (black lines) numbered $\lambda = 1$, $\lambda = 2$, etc. (The index λ is used to distinguish measurements acquired from different bedding planes on the same rock, listed in Tables 2–5.) Each pixel in the stereo image pair and each position in the stereo-derived DEM has a "look-vector" (red lines) that defines a ray to the corresponding position in the scene. The estimated surface positions (yellow stars), computed from stereo-derived disparities, are scattered along the look-vectors, overshooting or undershooting the true position (red stars). If the error is large enough, then a plane fitted to the sampled point cloud will be parallel to the look-vectors (i.e., called the "look-plane") instead of the true bedding plane. This tendency is measured by the "look-plane proximity" (κ) as described in Appendix A. (For interpretation of the references to color in this figure legend, the reader is referred to the web version of this article.)

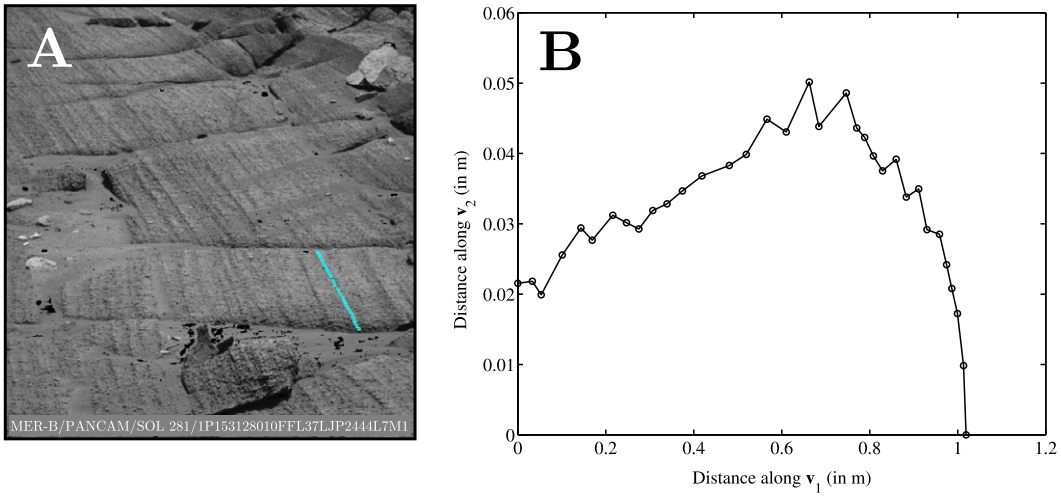

Fig. 24. (A) Cropped portion of a left-eye Pancam image from sol 281. Cyan dots mark points sampled along a bedding plane from a DEM created using this image and its right-eye counterpart. The sampled line spans 1 m. (B) The point cloud from the DEM queried in part A, plotted in the plane spanned by the first ($\mathbf{v}_1$) and second ($\mathbf{v}_2$) principal components. The third principal component, in the direction of least variation, is normal to the page. In this case, because the sampled points in image-space (part A, at left) form an almost perfectly straight line, the look-plane proximity, κ, is nearly zero: i.e., the fitted plane corresponds to the look-plane. However, the inter-point deviation is small ($\xi = 0.45$). That is, the ≈5 cm of relief corresponds to a real topographic surface rather than quasi-random variation along the look-vectors. The latter case is the result of errors in range estimates, and would appear as a ragged line with little or no recognizable shape. These data were acquired from bedding plane $\lambda = 1$ on rock $n_{\text{rock}} = 22$ in image img = 63 (see Table 4). (For interpretation of the references to color in this figure legend, the reader is referred to the web version of this article.)

ble 3, and at Burns Cliff in Tables 4 and 5. The contents of these tables are also plotted in Fig. 1, where in part A the rocks are number-labeled and color-coded to indicate the dip angle.

In overview, planes are fitted to point clouds sampled from digital elevation models (DEMs) of the local topography. These DEMs are generated from Navcam and Pancam stereo image pairs using the suite of VICAR stereo correlation programs such as Marscorr (Lorre and Deen, 1999). For each feature that Marscorr matches in both images of a stereo pair, a "binocular disparity" is computed. This disparity is the difference in apparent position of an object owing to the separation of the stereo cameras. From this disparity and the baseline length, a distance or "range" is computed along a ray called the "look-vector" (see Fig. 23). Errors in the computed topography therefore correspond to an uncertainty in position along the look-vectors.

Point clouds are sampled from bedding planes and a principal component analysis (PCA) is used to find the first and second principal components ($\mathbf{v}_1$ and $\mathbf{v}_2$, respectively). These vectors span the plane of greatest spatial variation of points in the cloud (see Fig. 24). The third principal component ($\mathbf{v}_3$) is normal to this plane, and the strike and dip are calculated from this vector. Dip is the angle that $\mathbf{v}_3$ makes with the vertical, and strike is the azimuth of the horizontal component of $\mathbf{v}_3$, minus 90°. The direction to North and the orientation of the vertical are determined by the position of the Sun and by onboard accelerometers, respectively.

To estimate the error in strike (φ) and dip (ϑ) we use a standard statistical method called a "bootstrap" analysis (Press et al., 1988). First, the distances from all points in the cloud to the fitted plane along the look-vectors are tabulated (we call this the set of distances $\mathbf{\Lambda}$), along with the points of intersection (i.e., the intersection of (a) the line determined by each point and its look-vector with (b) the fitted plane). For each point in a bootstrap-simulated cloud, a distance is sampled at random and with replacement from $\mathbf{\Lambda}$ and added to one of the intersection points along the corresponding look-vector. For each simulated cloud, a plane is fitted using PCA and the strike and dip are tabulated. This is repeated for 1000 simulated clouds.

By convention, dip is measured rightward of strike and ranges from 0° to 90°. The domain of dips must therefore be unfolded with respect to a reference strike so that median values and other statistics can be computed. Structural dip has the domain [0°,90°), and this is unfolded to [−45°,135°) with respect to a reference strike; if this were not done, a median dip of 0° (or near zero) would be precluded. The reference strike is modal, and corresponds to the tallest bin in a histogram of strikes for the 1000 bootstrap-simulated point clouds.

In Tables 2–5 we report the median strike and dip from the bootstrap distribution, as well as the range of the 95% confidence interval above ($\Delta\varphi_+$, $\Delta\vartheta_+$) and below ($\Delta\varphi_-$, $\Delta\vartheta_-$) the median values. We have reported median values instead of mean values so that the 95% confidence interval can be centered on the reported estimate (i.e., 50% lies above and 50% lies below), and to diminish the influence of outliers. In Tables 2–5, the mean value of dip differs from the median by <1° in all cases. The mean value of strike differs from the median by <1° in all but 13% of cases, and by <5° in all cases.

We can explicitly confirm that a point cloud is not more linear than planar in overall shape. In Tables 2–5 we report the "aspect ratio" (γ), defined as the ratio of variance along the third principal component to the variance along the second component. If γ is close to 1, the points in the cloud are collinear. Small values of γ indicate a planar shape.

Because the errors in topography correspond to uncertainty in position along the look-vectors, it is important to confirm that the fitted plane is not just determined by errors in the range estimates. We have addressed this problem in several ways.

(1) Points on a straight line in the image space (i.e., a straight line of pixels in the image used to query the DEM) always lie on a plane in 3-D space, provided there is topographic relief or scatter along the look-vectors. For this reason, unless it was clear from the image that a straight line (in image space) was traced from a surface with significant relief (such as where rounding a corner), straight-line samples were not acquired.

(2) We compute the "fraction of inter-point deviation" (ξ) defined as the mean of distances between nearest-neighbors along the second principal component, divided by the overall standard deviation of position along the second principal component. If $\xi \geqslant 1$, most of the variation along the second component

can be attributed to inter-point variation – usually a ragged curve, owing to large errors in range. If $\xi < 1$, most of the variation along the second component can be attributed to the overall shape of the point cloud – usually a smooth curve, reflecting the actual topography. See Fig. 24 for an example.

(3) We also calculate the orientation of the "look-plane." The look-plane is the plane fitted (using PCA) to a composite of the point cloud in three positions displaced along the look-vectors by one cloud span (defined as the largest distance between any two points in the cloud). The look-plane is therefore equivalent to a plane determined entirely by errors in the range estimates. If the plane fitted to the original point cloud has the same orientation as the look-plane, then it is likely also to be entirely determined by the errors in the stereo-derived range rather than variations in topography (unless $\xi < 1$).

In Tables 2–5 we report the "look-plane proximity" (κ, computed using the bootstrapped fits described above). Note that the normals of all planar fits can be represented as positions in spherical coordinate space. The quantity κ is the ratio of two "distances" in spherical coordinate space: (a) the distance (in radians) of the look-plane normal to the nearest bootstrap normal, over (b) the largest nearest-neighbor distance of any two normals in the cluster of bootstrapped normals. That is, if $\kappa \leqslant 1$ then the look-plane resides within the distribution of bootstrap realizations and is statistically indistinguishable from the original point-cloud fit. (In this case, if $\xi \geqslant 1$, the planar fit is very likely to be determined by errors in range.) If $\kappa > 1$, then the look-plane occurs outside the cluster of bootstrap-simulated normals. In that case, the planar fit to the original point cloud is statistically distinct from the look-plane, and therefore is probably not determined by errors in range estimates. In Tables 2–5 and Fig. 1 we have reported the results for all point clouds for which the 95% confidence interval in dip spans less than 20° ($\Delta\vartheta_+ + \Delta\vartheta_- < 20°$) and (a) whose fraction of inter-point deviation is less than one ($\xi < 1$) or (b) whose look-plane proximity is greater than one ($\kappa > 1$).

The topography in most locations dips between 20° and 35° craterward. Except downslope from the α structure in Fig. 3, this differs by at least 20° from the measured dip of bedding (i.e., by the span of the 95% confidence interval). In no case do we have reason to suspect that the measured structural dip has been mistaken for the slope of the surrounding topography. Sampled bedding planes range in length from several centimeters to 1 m. All were therefore smaller than the scale of deformation caused by the cratering flow, and all were measured from individual fault- and fracture-bounded rocks.

References

Arvidson, R.E. et al., 2004. Localization and physical property experiments conducted by opportunity at Meridiani Planum. Science 306, 1730–1733.

Barosh, P.J., 1968. Relationships of explosion-produced fracture patterns to geologic structure in Yucca Flat, Nevada test site. In: Eckel, E.B. (Ed.), Nevada Test Site, vol. 110. Geological Society of America, Boulder, CO, USA, pp. 199–217.

Barringer, D.M., 1905. Coon Mountain and its crater. Proc. Acad. Natl. Sci. Philadelphia 57, 861–886.

Bell, J.F. et al., 2003. Mars Exploration Rover Athena Panoramic Camera (Pancam) investigation. J. Geophys. Res. 108. doi:10.1029/2003JE002070.

Brandt, D., Reimold, W.U., 1995. The geology of the Pretoria Saltpan impact structure and the surrounding area. South African J. Geol. 98, 287–303.

Carlson, R.H., Jones, G.D., 1965. Distribution of ejecta from cratering explosions in soils. J. Geophys. Res. 70, 1897–1910.

Carter, N.L., 1968. Basal quartz deformation lamellae – A criterion for recognition of impactites. In: French, B.M., Short, N.M. (Eds.), Shock Metamorphism of Natural Materials. Mono Book Corp., Baltimore, pp. 453–474.

Chao, E.C., Shoemaker, E.M., Madsen, B.M., 1960. First natural occurrence of Coesite. Science 132, 220–222.

Dence, M.R., 1968. Shock zoning at Canadian craters: Petrography and structural implications. In: French, B.M., Short, N.M. (Eds.), Shock Metamorphism of Natural Materials. Mono Book Corp., Baltimore, pp. 169–184.

Eppler, D.T., Nummedal, D., Ehrlech, R., 1977. Fourier analysis of lunar crater shape – Possible guide to impact history and lunar geology. In: Roddy, D.J., Pepin, R.O., Merrill, R.B. (Eds.), Impact and Explosion Cratering. Pergamon Press, New York, New York, pp. 511–526.

Evans, G.L., 1961. Investigations at the Odessa Meteor Craters. In: Proceedings of the Geophysical Laboratory – Lawrence Radiation Cratering Symposium, vol. 1, pp. D1–D11.

Evans, G.L., Mear, C.E., 2000. The Odessa meteor craters and their geological implications. Occasional papers of the Strecker Museum, vol. 5. Baylor University, Waco, TX, USA.

Fulmer, C.V., Roberts, W.A., 1963. Rock induration and crater shape. Icarus 2, 452–465.

Gault, D.E., Quaide, W.L., Oberbeck, V.R., 1968. Impact cratering mechanics and structures. In: French, B.M., Short, N.M. (Eds.), Shock Metamorphism of Natural Materials. Mono Book Corp., Baltimore, MD, pp. 87–99.

Grant, J.A. et al., 2006. Crater gradation in Gusev crater and Meridiani Planum. Mars. J. Geophys. Res. 1–23.

Grant, J.A., Wilson, S.A., Cohen, B.A., Golombek, M.P., Geissler, P.E., Sullivan, R.J., Kirk, R.L., Parker, T.J., 2008. Degradation of Victoria Crater, Mars. J. Geophys. Res. 113. doi:10.1029/2008JE003155.

Grotzinger, J.P. et al., 2005. Stratigraphy and sedimentology of a dry to wet eolian depositional system, Burns formation, Meridiani Planum, Mars. Earth Planet. Sci. Lett. 240, 11–72.

Guppy, D.J., Brett, R., Milton, D.J., 1971. Liverpool and Strangways craters, Northern Territory: Two structures of probable impact origin. J. Geophys. Res. 76, 5387–5393.

Hayes, A.G., Grotzinger, J.P., Edgar, L., Watters, W.A., Squyres, S., Sohl-Dickstein, J., 2010. Reconstruction of eolian bedforms from cross-bedded strata at Victoria Crater, Mars. J. Geophys. Res., submitted for publication.

Herkenhoff, K.E. et al., 2004. Evidence from Opportunity's microscopic imager for water on Meridiani Planum. Science 306, 1727–1730.

Herkenhoff, K.E. et al., 2008. Surface processes recorded by rocks and soils on Meridiani Planum, Mars: Microscopic imager observations during Opportunity's first three extended missions. J. Geophys. Res. 113. doi:10.1029/2008JE003100.

Hörz, F., 1968. Statistical measurements of deformation structures and refractive indices in experimentally shock-loaded quartz. In: French, B.M., Short, N.M. (Eds.), Shock Metamorphism of Natural Materials. Mono Book Corp., Baltimore, pp. 243–253.

Knoll, A.H. et al., 2008. Late diagenetic veneers, rinds, and fracture fill at Meridiani Planum, Mars. J. Geophys. Res. 113. doi:10.1029/2007JE002949.

Kring, D.A., 2007. Guidebook to the Geology of Barringer Meteorite Crater, Arizona, first ed. Lunar and Planetary Institute, Houston, Texas.

Kumar, P.S., 2005. Structural effects of meteorite impact on basalt: Evidence from Lonar crater, India. J. Geophys. Res.. doi:10.1029/2005JB003662.

Kumar, P.S., Kring, D., 2008. Impact fracturing and structural modification of sedimentary rocks at Meteor Crater, Arizona. J. Geophys. Res. 113. doi:10.1029/2008JE003115.

Lafond, E.C., Dietz, R.S., 1964. The Lonar Crater, India, a meteorite crater? J. Indian Geophys. Union 1, 91–97.

Li, R. et al., 2007. Opportunity rover localization and topographic mapping at the landing site of Meridiani Planum, Mars. J. Geophys. Res., 1–12.

Lorre, J., Marscorr, Deen B., 1999. JPL-MIPL VICAR Planetary Image Processing Package.

Maki, J.N. et al., 2003. Mars Exploration Rover Engineering Cameras. J. Geophys. Res. 108. doi:10.1029/2003JE002007.

Maloof, A.C., Stewart, S.T., Soule, S.A., Weiss, B.P., Swanson-Hysell, N.L., Louzada, K.L., Garrick-Bethell, I., Poussart, P.M., 2009. Geology of Lonar Crater, India. GSA Bull. 122, 109–126. doi:10.1130/B26474.1.

Maxwell, D.E., 1977. Simple Z model of cratering, ejection, and the overturned flap. In: Roddy, D.J., Pepin, R.O., Merrill, R.B. (Eds.), Impact and Explosion Cratering. Pergamon Press, New York, pp. 983–1022.

McEwen, A.S., Preblich, B.S., Turtle, E.P., Artemieva, N.A., Golombek, M.P., 2005. The rayed crater Zunil and interpretations of small impact craters on Mars. Icarus 176, 351–381.

McGetchin, T.R., Settle, M., Head, J.W., 1973. Radial thickness variation in impact crater ejecta: Implications for lunar basin deposits. Earth Planet. Sci. Lett. 20, 226–236.

McLennan, S.M. et al., 2005. Provenance and diagenesis of the evaporite-bearing Burns formation, Meridiani Planum. Mars. Earth Planet. Sci. Lett. 240, 95–121.

Melosh, M.J., 1989. Impact Cratering: A Geological Process, first ed. Oxford Univ. Press, New York.

Milton, D.J., 1968. Structural Geology of the Henbury Meteorite Craters, Northern Territory, Australia. Geological Survey Professional Papers 599-C, pp. C1–C17.

Milton, D.J., Michel, F.C., 1965. Structure of a Ray Crater at Henbury, Northern Territory, Australia. Geological Survey Professional Papers 525-C, pp. C5–C11.

Piekutowski, A.J., 1977. Cratering mechanisms observed in laboratory-scale high-explosive experiments. In: Roddy, D.J., Pepin, R.O., Merrill, R.B. (Eds.), Impact and Explosion Cratering. Pergamon Press, New York, pp. 67–102.

Pilon, J.A., Grieve, R.A.F., Sharpton, V.L., 1991. The subsurface character of Meteor Crater, Arizona, as determined by ground-probing radar. J. Geophys. Res. 96, 15563–15576.

Poelchau, M.H., Kenkmann, T., Kring, D.A., 2009. Rim uplift and crater shape in Meteor Crater: Effects of target heterogeneities and trajectory obliquity. J. Geophys. Res. 114. doi:10.1029/2008JE003235.

Press, W.H., Teukolsky, S.A., Vetterling, W.T., Flannery, B.P., 1988. Numerical Recipes in C, second ed. Cambridge Univ. Press, Cambridge, UK.

Regan, R.D., Hinze, W.J., 1975. Gravity and magnetic investigations of Meteor Crater, Arizona. J. Geophys. Res. 80, 776–778.
Roddy, D.J., 1978. Pre-impact geologic conditions, physical properties, energy calculations, meteorite and initial crater dimensions and orientations of joints, faults and walls at Meteor Crater, Arizona. Lunar Planet. Sci. 9, 3891–3930.
Roddy, D.J., Boyce, J.M., Colton, G.W., Dial. A.L., 1975. Meteor Crater, Arizona, rim drilling with thickness, structural uplift, diameter, depth, volume, and mass-balance calculations. Proc. Lunar Sci. 6, 2621–2644.
Shoemaker, E.M., 1960. Penetration mechanics of high velocity meteorites, illustrated by Meteor Crater, Arizona. In: International Geological Congress, 21.
Shoemaker, E.M., 1963. Impact mechanics at Meteor Crater, Arizona. In: Middlehurst, B.M., Kuiper, G.P. (Eds.), The Moon, Meteorites, and Comets. University of Chicago Press, 1963, pp. 301–306.
Shoemaker, E.M., Eggleton, R.E., 1961. Terrestrial features of impact origin. In: Proceedings of the Geophysical Laboratory – Lawrence Radiation Cratering Symposium, vol. 1, pp. A1–A27.
Shoemaker, E.M., MacDonald, F.A., Shoemaker, C.S., 2005. Geology of five small Australian impact craters. Aus. J. Earth Sci. 52, 529–544.
Smith, R., 2006. The Open Dynamics Engine v0.5 User Guide, first ed.
Soderblom, L.A. et al., 2004. Soils of Eagle Crater and Meridiani Planum at the Opportunity rover landing site. Science 306, 1723–1726.
Squyres, S.W. et al., 2009. Exploration of Victoria Crater by the Mars Opportunity Rover. Science 324, 1058–1061.
Stoeffler, D., Gault, D.E., Wedekind, J., Polkowski, G., 1975. Experimental hypervelocity impact into quartz sand: Distribution and shock metamorphism of ejecta. J. Geophys. Res. 80, 4062–4077.
Sullivan, R. et al., 2005. Aeolian processes at the Mars Exploration Rover Meridiani Planum landing site. Nature 436, 58–61.
Watters, W.A., 2009. Hypervelocity Impacts and the Evolution of Planetary Surfaces and Interiors. MIT PhD thesis, Cambridge, MA, USA.